



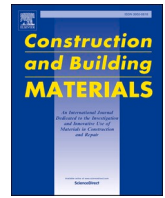
Cross laminated timber with air gaps in cross-layers: Numerical analysis and experimental evaluation

Downloaded from: <https://research.chalmers.se>, 2025-06-01 14:04 UTC

Citation for the original published paper (version of record):

Tahmasebi, M., Kurzawinska, H., Jockwer, R. et al (2025). Cross laminated timber with air gaps in cross-layers: Numerical analysis and experimental evaluation. *Construction and Building Materials*, 481. <http://dx.doi.org/10.1016/j.conbuildmat.2025.141577>

N.B. When citing this work, cite the original published paper.



Cross laminated timber with air gaps in cross-layers: Numerical analysis and experimental evaluation

Mohammad Tahmasebi^a, Hanna Kurzawinska^a, Robert Jockwer^b, Yutaka Goto^{a,*}

^a Department of Architecture and Civil Engineering (ACE), Chalmers University of Technology, Gothenburg SE 412 96, Sweden

^b Faculty of Civil Engineering, Dresden University of Technology, Dresden 01062, Germany

ARTICLE INFO

Keywords:

Cross-laminated timber
CLT
Material reduction
Rolling shear strength
Bending stiffness
Modified gamma method

ABSTRACT

Cross-laminated timber (CLT) panels are favored for their lightweight nature and widespread applications in construction. However, there are concerns that the production of these panels may involve excessive raw material usage relative to the structural requirements in specific scenarios. This paper investigates the structural implications of incorporating air gaps within the cross layers of CLT panels, with a focus on their potential to enhance material efficiency without compromising load-bearing capacity. Various configurations, including solid panels and panels with centrally and shifted arrangements of voids in different sizes, were examined. Employing experimental testing and numerical analysis, the study explores variations in rolling shear strength, bending stiffness, and deflection across CLT panel configurations. Shear tests on a small scale and four-point bending tests at a full scale were conducted on CLT panel samples. The findings reveal that the presence of air gaps significantly impacts the structural properties of CLT panels. Among the different configurations tested with air gaps between lamellas in cross layers, those with lamellas, whose center is shifted relative to each other with the highest overlap across different cross layers exhibited greater rolling shear strength. This underscores the importance of the strategic placement of air gaps in refining CLT panel design for both efficiency and performance. Additionally, the study introduces adjusted smeared shear modulus values for the CLT panels with air-gaped configurations, which are correlated with solid panel properties. In four-point bending tests, it was observed that panels with wider air gaps showed increased deflection and decreased stiffness compared to solid panels without air gaps. The study suggests that the stiffness of CLT panels with air gaps can be effectively predicted using the modified gamma method when incorporating the adjusted rolling shear modulus into calculations. Furthermore, the Timoshenko method requires adjusting the shear correction factor, κ_s , to predict beam deflection effectively.

1. Introduction

Wood is a common construction material for both traditional and modern constructions in many areas of the world. While it has advantages in its lightweight nature, renewability, etc., the dimension of logs and the anisotropic characteristics are limited to its biological growth characteristic. In order to overcome such disadvantages, a number of engineered wood products have been developed and deployed in timber structures over the past century. Among these, cross-laminated timber (CLT) panels have garnered attention for their superior load-bearing capacity and environmental benefits when compared to conventional construction materials such as steel or concrete [1]. CLT was developed as a high-value product for the use of sideboards. A comprehensive and

in-depth review and development of the CLT panels can be found in [2]. The first European standard for CLT was published in 2015 and the design of CLT structure will be included in the next generation of the European design code for timber structures EN 1995-1-1 [3].

Research by Ben Toosi [4] showed that around 70 percent of the production cost for a CLT panel is for raw materials. Another research [5] suggests that this cost percentage can decrease to roughly 59 %. While the current CLT production method is focused on the simple process of the assembly and press of the lamellas for a massive panel, there is room for improvement in material efficiency in certain scenarios. There is a high potential in the raw material reduction especially in the center and core sections of CLT panels as it contributes minimally to the structural performance in bending. It means that there might be

* Corresponding author.

E-mail address: yutaka@chalmers.se (Y. Goto).

<https://doi.org/10.1016/j.conbuildmat.2025.141577>

Received 1 July 2024; Received in revised form 22 April 2025; Accepted 29 April 2025

Available online 6 May 2025

0950-0618/© 2025 The Author(s). Published by Elsevier Ltd. This is an open access article under the CC BY license (<http://creativecommons.org/licenses/by/4.0/>).

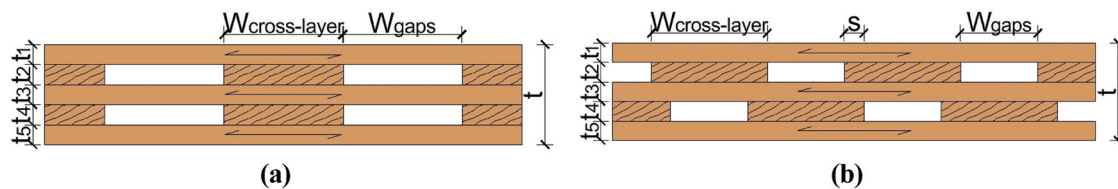


Fig. 1. The illustration of the CLT panels with air gaps: (a) Central arrangements, (b) Shifted arrangement.

no need to form a simple massive panel, and instead, the timber lamellas can be arranged properly with gaps in between while maintaining the required load-bearing capacity.

To investigate the impact of introducing air gaps within the cross layers, a number of geometric factors can be taken into consideration, such as the number of layers, the thickness of each layer, the width of lamellas in the cross layers, and the arrangement of air gaps in relation to the air gaps in other layers whether they are centrally positioned (Fig. 1a) or shifted (Fig. 1b).

Franzoni et al. [6] investigated the influence of spacing between narrow boards in cellular CLT panels. Their findings indicated that the bending stiffness decreases as the space between lamellas increases, following the wood volume fraction within the panel. However, they found that when addressing transverse shear stiffness related to out-of-plane behavior, the reduction of stiffness with spacing does not follow the volume fraction. Silly et al. [7] showed the possible options for the optimization of the CLT panels. They explained that there are some advantages of using air gaps between cross layers, such as a significant reduction of material and the possibility of using these spaces to improve insulation and acoustic properties. On the other hand, it leads to raising new questions regarding the design process and a significant reduction of shear strength and transverse bending stiffness. Therefore, incorporating air gaps in the cross layers within CLT panels has the potential to lower the use of raw materials, decrease environmental impact, and make them an alternative to conventional CLT panels. However, uncertainties surrounding their structural performance remain a significant concern.

Generally, CLT panel behavior under out-of-plane loads is assessed through various analytical methods, including the K-method, the Modified Gamma method (referred to as the gamma method in this paper), the Timoshenko method, and the Shear Analogy method.

The K-method, introduced by Fellmoser and Blaß [8], employs the “Composite Theory” to forecast the strength and stiffness of CLT. However, it is crucial to note that the K-method does not account for shear deformation in individual layers. Nevertheless, it exhibits reasonable accuracy for elements having a high span-to-depth ratio

$$\left(\frac{l_{CLT}}{h_{CLT}} \geq 30 \right) [9].$$

In the gamma method, the cross-layer is modeled as being semi-rigidly connected between two longitudinal layers. To capture shear deformation in the cross-layer, a slip factor (γ) is introduced, which depends on the rolling shear modulus. This concept is based on the mechanically jointed beam theory from Eurocode 5, Annex B. When applied to cross-laminated timber, each longitudinal layer is treated as an individual beam. The connection between the layers is represented by Gamma factors (γ), which account for shear deformation in the transverse layers. These Gamma factors reduce the second term of Steiner’s theorem for the longitudinal layers. The moment of inertia, adjusted using these factors, is called the effective moment of inertia. This effective moment of inertia is then used in the equations for deformations according to Bernoulli-Euler beam theory [10,11].

Timoshenko beam theory extends the Bernoulli-Euler beam theory by incorporating shear deformation, making it more suitable for analyzing thick beams. Unlike Bernoulli-Euler theory, which assumes that cross-sections remain straight and perpendicular to the neutral axis during deformation, Timoshenko theory allows for cross-sectional

rotations due to shear deformation. When applied to cross-laminated timber, Timoshenko theory typically considers only the longitudinal layers as contributing to the moment of inertia, based on the assumption that the transverse layers have zero normal stiffness, this is known as the net moment of inertia. Additionally, shear deformation is addressed using a shear correction factor, which compensates for the uneven distribution of shear strain across the cross-section [12–14].

The Shear Analogy method, although relatively complex, involves separating the multi-layer CLT into two virtual beams with equal vertical deformation. This allows obtaining the material properties of the entire CLT by overlaying the performance of both beams [15].

A comparative analysis of Timoshenko, shear analogy, and gamma methods is provided by Bogensperger et al. [16]. According to this analysis, it was concluded that they do not greatly differ for practical (single) spans $\frac{l_{CLT}}{h_{CLT}} \geq 15$, and each of these methods can, in fact, be applied [17]. Therefore, this paper employs the Timoshenko and gamma methods for analytical calculations of stiffness and deflection.

There is limited research on the impact of introducing air gaps between cross layers on the structural behavior of CLT panels. Previous studies have primarily focused on introducing air gaps in a central arrangement and evaluating bending stiffness [6,7,18]. However, there is a lack of research regarding the effect of air gaps between cross layers on shear strength and modulus.

The primary objective of the research is to evaluate the structural performance of five-layer CLT panels by examining how varying air gap sizes and cross-layer configurations affect their rolling shear strength and modulus. The study also included comprehensive testing on large-scale samples, emphasizing deflection and bending stiffness through out-of-plane four-point bending tests. These tests focused on assessing the elastic properties and stiffness of the CLT panels, with the results compared using equations incorporating the rolling shear modulus and shear correction factors derived from the shear tests.

To guide this investigation, the paper addresses two key sets of research questions:

1. Shear analysis:
 11. How do air gap size and cross-layer arrangement influence overall shear strength?
 12. How does the overall shear modulus of a CLT panel respond to changes in air gap dimensions and arrangement?
 13. What smeared shear modulus values can be applied to CLT panels with air gaps, compared to solid CLT panels?
2. Four-point bending analysis:
 21. Can a simple analytical approach such as the gamma method accurately predict the stiffness of CLT panels with air gaps between lamellas in the cross layers?
 22. How accurately can deflection be predicted using analytical methods such as Timoshenko and gamma methods, in comparison to FEM models and experimental results?

This study focuses on five-layer CLT panels, where each lamella has a consistent thickness of 20 mm, and the lamellas in the cross layers have a width of 120 mm. The research explores different arrangements of cross layers, including air gap sizes (W_{gaps}) equal to 60 and 120 mm for central configurations (see Fig. 1a), and for shifted arrangements with

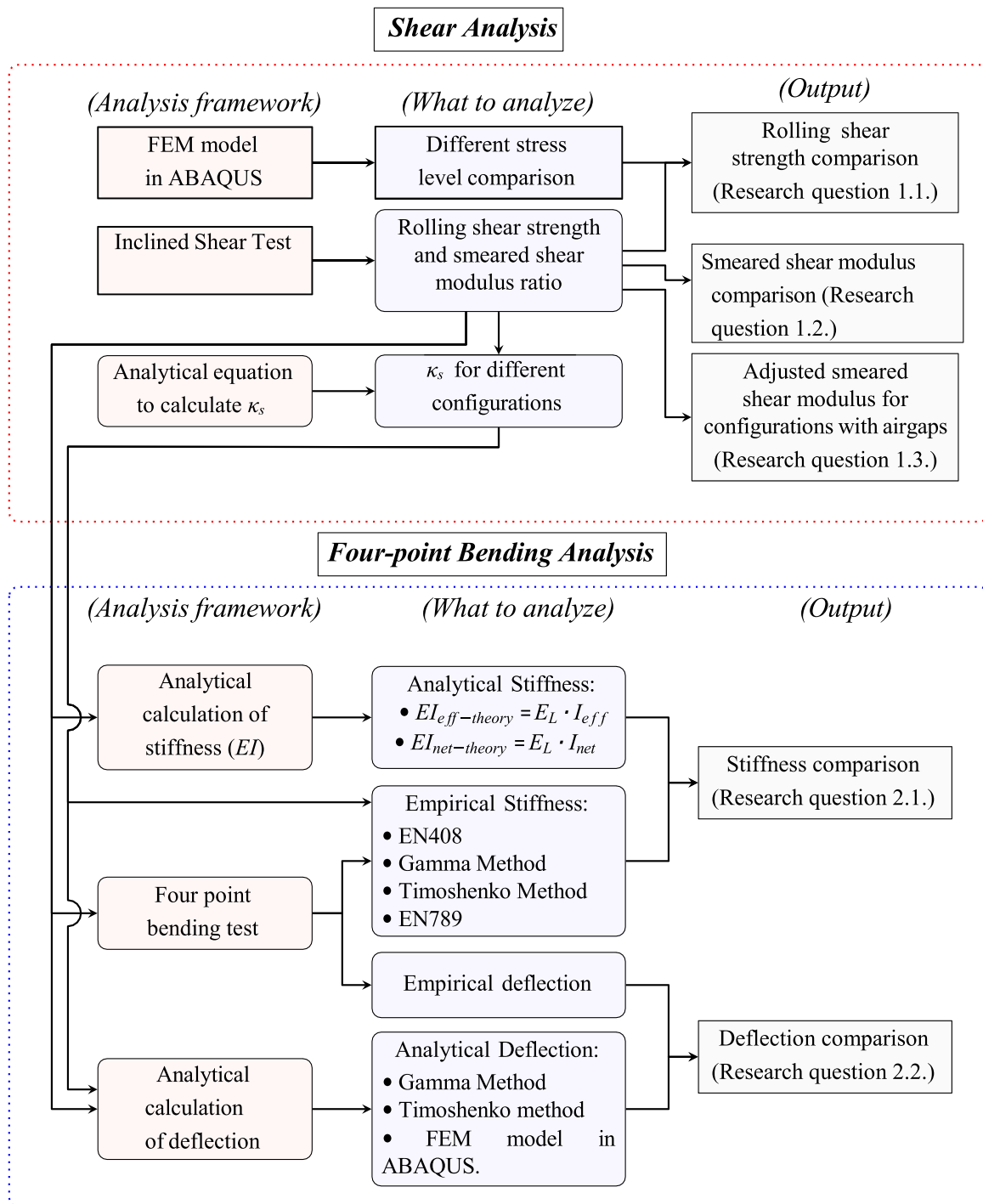


Fig. 2. Flowchart to show the sequential steps in this study.

overlapping dimensions (S) equal to zero, 20, and 30 mm (see Fig. 1b).

2. Methodology

2.1. Overall framework of methodology

This study proposes a selective reduction of the core layer in CLT panels by introducing gaps between lamellas of the cross layers. The investigation explores the impact of this modification on overall rolling shear strength and smeared shear modulus of the CLT panel, proposing new values for the shear modulus of configurations with air gaps relative to solid CLT panels. To gain insights, a finite element model in ABAQUS

was employed. Subsequently, four-point bending tests assessed stiffness, comparing them with solid CLT panels and analytical calculations. Finally, deflection curves obtained from the experiments were compared with FEM simulation and analytical models to evaluate their accuracy. The sequential steps employed in this study are outlined in the flowchart presented in Fig. 2.

The tests in this study were specifically designed for a five-layer CLT configuration to evaluate the structural performance of the entire panel, rather than the properties of individual lamellas. The reported shear and bending stiffness values characterize the global behavior of the CLT panels. While the term "smeared" is used where necessary for clarity, all reported mechanical properties should be understood as representing

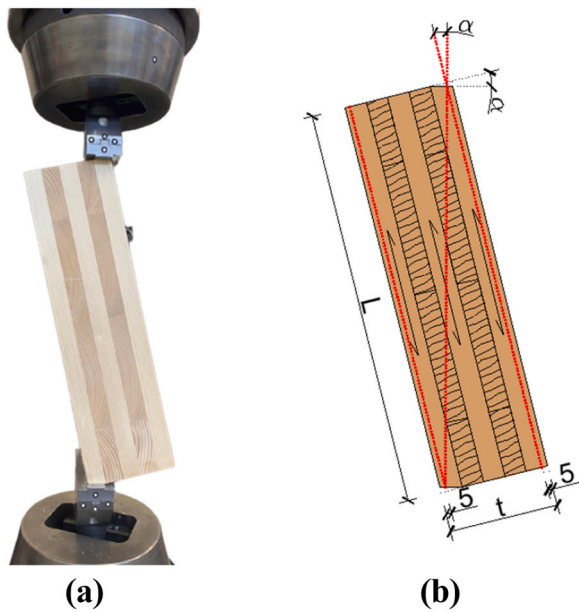


Fig. 3. (a) The shear test setup, (b) The illustration of the specimen with sawn edges.

panel-level (smeared) behavior, even when not explicitly stated. The findings of this study are specific to the tested five-layer CLT configurations with predefined air gap arrangements and material properties. While they provide valuable insights into the structural behavior of CLT panels with air gaps, the results should not be directly extrapolated to all five-layer CLT panels, as variations in lay-up patterns, wood species, adhesive type, and manufacturing processes may influence rolling shear stiffness and overall performance.

2.2. Shear test

EN 16351 [19], specifies that the rolling shear strength and stiffness of CLT panels should be assessed using a test configuration that includes a single cross-layer and applies loading parallel to the longitudinal layers. However, in this study, an inclined shear-compression test was conducted on five-layer CLT specimens containing two cross-layers, following a modified approach inspired by the general methodology in EN 16351 and EN 408 [20], (see Fig. 3a). This adaptation allowed for the calculation of a shear stiffness across the entire CLT panel, representing the combined shear response of multiple layers, which provides a more realistic assessment of shear behavior in practical applications.

The specimens were cut at an angle along the outer lamellas' opposing edges to ensure parallel forces along the intended shear plane and to prevent bending from off-axis forces. The cutting angle α ,

calculated using Eq. 1, varied across configurations due to differences in specimen dimensions, influenced by the arrangement of cross-layers and air gaps, where t is the total thickness and L is the length, both in mm. This inclination angle α facilitated proper attachment of the specimens in the hydraulic press and was specifically chosen to create a shear force component parallel to the grain while minimizing perpendicular-to-grain stresses.

$$\alpha = \arctan\left(\frac{t - 2.5\text{mm}}{L}\right) \quad (1)$$

The thickness was reduced by 5 mm on each side to improve alignment of the specimen's vertical axis rather than centering the axis within the outer layers. This adjustment aimed to align the vertical axis more precisely with the intended loading direction in the hydraulic press. This approach was selected to minimize eccentricities and ensure that the applied loads acted along the vertical axis, reducing potential bending effects during testing, see Fig. 3b. To secure this condition during testing, the specimens were consistently aligned in the hydraulic press. The outer edge of the bottom pressure area was aligned with one edge of the pressure plate, and similarly, the top pressure plate was aligned with the outer edge of the upper pressure area of the specimen, Fig. 4. This procedure helped ensure that the applied forces were transmitted centrally along the intended vertical axis, maintaining the offset alignment throughout the tests.

The shear test was conducted using the universal testing machine (type MTS Model 327.21) with a maximum capacity of 250 kN. The ARAMIS optical system [21] was utilized to capture surface deformations of the specimens, enabling the calculation of the corresponding strain, with measurements taken on only one side of the specimens. The surface of the specimen was pre-treated with a white matte paint to create a non-reflective, high-contrast background. A random pattern of black speckles was then applied to facilitate accurate tracking by the ARAMIS 3D optical measurement system, which calculates surface deformations based on grayscale image correlation. The system measures the displacement and strain fields by analyzing how the speckle pattern deforms during loading. To monitor the global deformation of fixed components, such as the hydraulic press, dedicated reference points were marked on these structures, as shown in Fig. 4.

The positioning of these reference points was consistent across all specimens to ensure accurate comparison and to track local deformations at critical locations. The system was initially configured to capture one image per second (1 Hz) upon the commencement of the loading process. Furthermore, the data acquisition for both load and deformation were saved using the MTS FlexTest software at each discrete step in the experiment. The loading rate is selected at 0.5 mm/min, and the maximum load was reached within the time in the range of 300 ± 120 s for all of the configurations. The rolling shear strength (f_r) and smeared shear modulus ($G_{smeared}$) were calculated, see Eqs. 2, and 3.

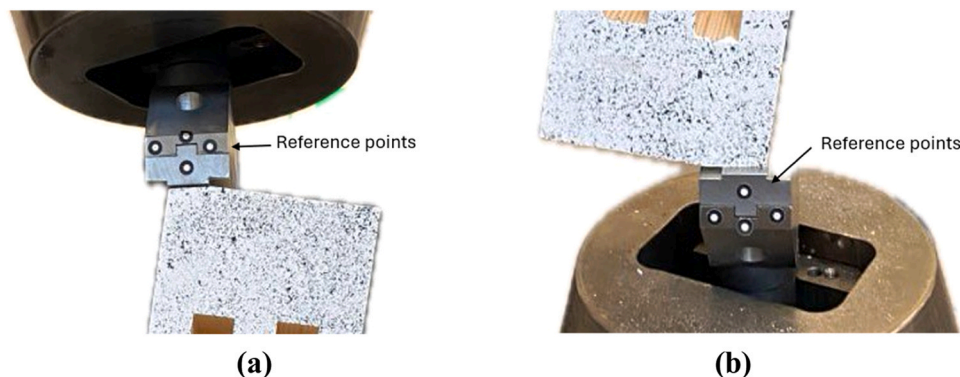


Fig. 4. Aligning of a specimen on the pressure plates in the hydraulic press during the shear test: (a) the top support, (b) The bottom support.

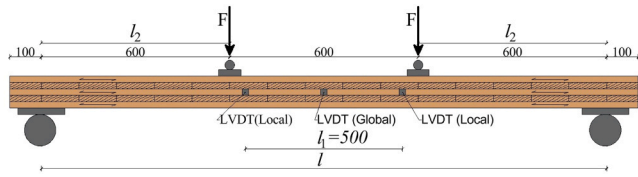


Fig. 5. The four-point bending test setup [mm].

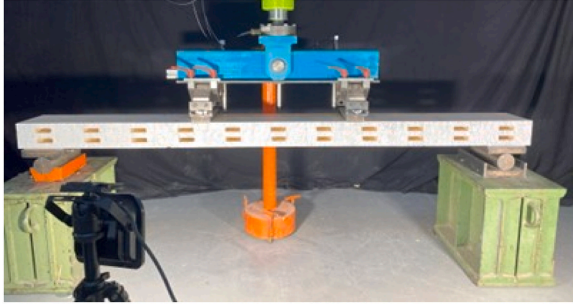


Fig. 6. The four-point bending test setup for configuration B.

$$f_r = \frac{F_{\max} \cdot \cos(\alpha)}{L \cdot b} \quad (2)$$

$$G_{\text{smear}} = \frac{(F_2 - F_1) \cdot t}{(u_2 - u_1) \cdot L \cdot b} \quad (3)$$

These equations comprise several variables: $(F_2 - F_1)$ for load increments ranging between $0.1 F_{\max}$ and $0.4 F_{\max}$ in [N], $(u_2 - u_1)$ representing deformation increments relative to $(F_2 - F_1)$ through linear regression in [mm] (The deformation u represents the displacement aligned with the direction of the applied force), b as the width of the test specimen in [mm], L as the total length of the test specimen in [mm], t denoting the thickness of the test specimen in [mm], and α indicating the angle between the load direction and the longitudinal axis, in degrees.

Both the calculated rolling shear strength (f_r) and shear modulus (G_{smear}) represent smeared values, reflecting the overall shear response of the CLT panel. Eq. 3 is based on the full specimen thickness and span length, resulting in a smeared shear modulus that captures the global behavior of the entire panel. This approach accounts for contributions from both longitudinal and transverse layers, as well as potential compressive effects, and does not isolate the material-level rolling shear properties of the transverse lamellas.

2.3. Four-point bending test

The four-point bending test was conducted according to EN 408. The tests were conducted using a flexible rig with one central hydraulic actuator and a load distribution beam. To achieve uniform load distribution across the specimen width and to avoid local compression, steel plates were placed at the supports (250×150 mm) and the load introduction points (250×70 mm). Although EN 408 specifies that the width of the plates at the support positions should not exceed half the depth of the test piece (50 mm), the steel plates' width at support was increased due to air gaps between the cross-layers near the supports. This modification aimed to minimize excessive stress concentrations in the support areas and provide a more uniform load distribution, thus avoiding potential localized failure, as illustrated in the Fig. 6. The distance from the load introduction point to the support was 600 mm (6 h), which was equivalent to the distance between the load introduction points. The supports were positioned 100 mm away from the ends of the specimens (see Fig. 5). The displacements at midspan and the load introduction points were measured using linear variable differential transformers (LVDTs). Half of the specimen from one end to midspan

was covered by the ARAMIS system. The loading rate was established displacement controlled at 5 mm/min. The load application occurred in three stages: initially, the load was increased until it reached approximately 40 percent of the anticipated load-bearing capacity of the beam, then it was reduced to 10 percent, and ultimately, the load was increased until the beam experienced failure.

The global bending stiffness of a homogeneous cross-section can be calculated by the EN 408, see Eq. 4, and also by Bernoulli and Timoshenko methods, Eqs. 5, and 6, respectively.

$$(EI)_{\text{global,EN408}} = \frac{l_2 \cdot (3l^2 - 4l_2^2)}{24 \cdot \left(\frac{(w_{g,2} - w_{g,1})}{(F_2 - F_1)} - \frac{6l_2}{5G \cdot b \cdot t} \right)} \quad (4)$$

$$(EI)_{\text{global,Bernoulli}} = \frac{l_2 \cdot (3l^2 - 4l_2^2)}{24} \cdot \frac{(F_2 - F_1)}{(w_{g,2} - w_{g,1})} \quad (5)$$

$$(EI)_{\text{global,Timoshenko}} = \frac{l_2 \cdot (3l^2 - 4l_2^2)}{24 \cdot \left(\frac{(w_{g,2} - w_{g,1})}{(F_2 - F_1)} - \frac{l_2}{\kappa_s \cdot G \cdot A_{\text{net}}} \right)} \quad (6)$$

In assessing global bending stiffness, both bending and shear effects are combined, providing a simplified analysis of the material's overall structural response. Conversely, for local bending stiffness determination in the four-point bending test, only the deflection between applied forces is considered, focusing solely on bending effects and excluding shear deformation considerations. The local bending stiffness of the beam was determined using the equation provided in EN 789 [22], see Eq. 7.

$$(EI)_{\text{local,EN789}} = \frac{(F_2 - F_1) \cdot l_2 \cdot l_1^2}{8 \cdot (w_{l,2} - w_{l,1})} \quad (7)$$

In the four equations above, the symbols represent the following: $(F_2 - F_1)$ stands for the load increment within the range of $0.1 F_{\max}$ and $0.4 F_{\max}$ in [N], $(w_{l,2} - w_{l,1})$ signifies the increments of local deflection corresponding to $F_2 - F_1$ in [mm], $(w_{g,2} - w_{g,1})$ denotes the increments of global deflection relative to $F_2 - F_1$, l_2 represents the distance between the support and the point load position in [mm], κ_s symbolizes the shear correction factor, l_1 denotes the distance between the LVDT sensors used for measuring local deflection in [mm], l refers to the distance between the beam support in [mm], b is the width of the test specimen in [mm], G represents the mean shear modulus in $[\text{N}/\text{mm}^2]$ which considered as to 650 MPa based on EN 408, and A_{net} is the net cross-sectional area, defined as $A_{\text{net}} = b \cdot t$, see Fig. 5.

The maximum deflection (w_{global}) of a beam in a four-point bending test setup as shown in Fig. 6 can be calculated using Eq. 8:

$$w_{\text{global}} = \frac{Fl_2 \cdot (3l^2 - 4l_2^2)}{24 \cdot E_L \cdot I_{\text{net}}} + \frac{F}{D_{GA}} \cdot l_2 \quad (8)$$

where, I_{net} represents the net moment of inertia in $[\text{mm}^4]$, dependent solely on longitudinal layers, assuming negligible stiffness contribution from transverse layers. Additionally, D_{GA} is defined by Eq. 9, where G_i denotes the shear modulus of the i -th layer in $[\text{N}/\text{mm}^2]$, and A_i signifies the area of the i -th layer in $[\text{mm}^2]$.

$$D_{GA} = \kappa_s \cdot \sum_{i=1}^n A_i G_i \quad (9)$$

2.4. FEM modeling

To compare experimental results with numerical analysis, FEM models were created using ABAQUS [23]. The layers of the CLT panel were modeled as 3D deformable elements, utilizing solid shapes and extrusion types. The elastic model behavior was set as orthotropic. The constraints were used to model interactions between neighboring layers.

In the FEM model for the shear test, a Load Scale Factor (LSF) was

Table 1
Mechanical properties of boards used in FE models in ABAQUS and MATLAB.

	Elastic Modulus [MPa]		Density [kg/m ³]	Poisson's Ratio [-]			Shear Modulus [MPa]	G_{RT}
	E_R	E_T	ρ	ν_{LR}	ν_{LT}	$\nu_{RT}G_{LR}$	G_{LT}	
E_L	11000	400	420	0.42	0.48	0.50690	690	50

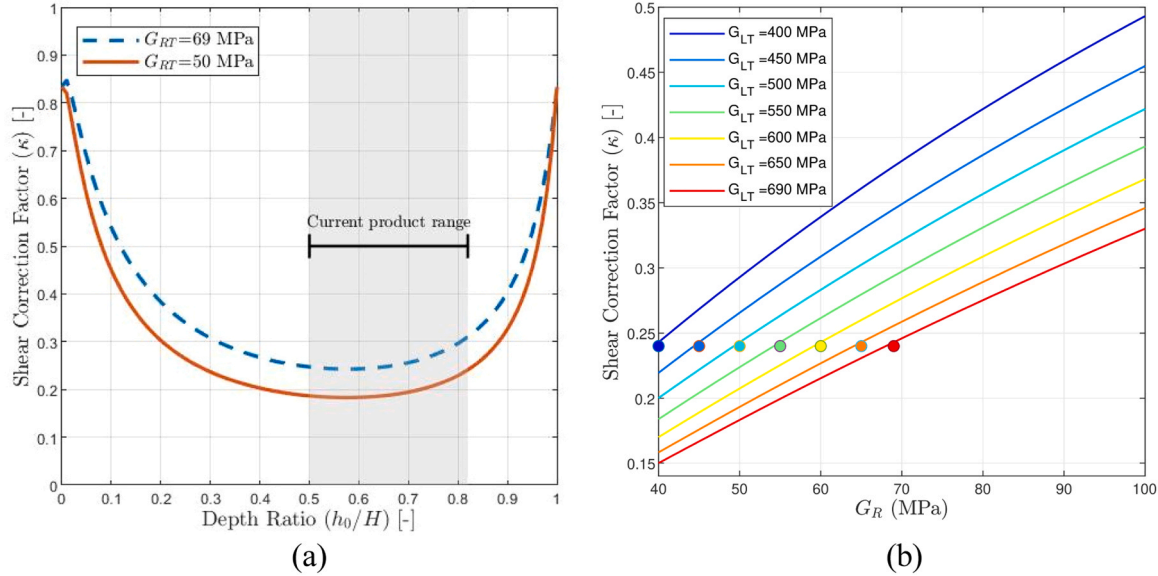


Fig. 7. (a) Analytical shear correction coefficient for a five-layer symmetrical CLT panel using C24 boards. Two sets assume rolling shear modulus values of 69 and 50 MPa, with h_0 as cumulative longitudinal layer thickness. (b) Relationship between κ and G_0 variations in a five-layer symmetrical CLT panel with uniform layer thickness, the outermost boards oriented longitudinally (Figure adapted from [32]).

introduced to account for variations

in specimen length and pressure area resulting from differences in geometry and cutting angles. This

adjustment ensured comparable stress fields and structural responses across configurations. Since all

specimens had the same width, this approach also led to an approximately constant average shear stress

$\left(\frac{F}{L \cdot b}\right)$. The LSF was calculated as the product of the length ratio (η_L) and the pressure area ratio (η_p), relative to the solid reference configuration, identified as Configuration I. The formulation of the LSF is presented in Eq. 10.

$$LSF = \eta_p \cdot \eta_L \tag{10}$$

Where η_L and η_p are the length and area ratio, defined as below:

$$\eta_L = \frac{L}{L_{ref}} \tag{11}$$

$$\eta_p = \frac{A_p}{A_{p,ref}} \tag{12}$$

where L and A_p represent the length and pressure area of the specific configuration, while L_{ref} and $A_{p,ref}$ denote the corresponding reference values from the solid configuration, with units of [mm] and [mm²], respectively.

The LSF values were set to 1.00 for Configuration I and to 1.48, 1.24, 1.32, 1.63, and 1.37 for Configurations II through VI, respectively. These values were used to scale the applied uniform pressure in the FEM model. By incorporating the LSF directly into the applied load, all configurations were analyzed under normalized loading conditions. This ensures that any observed differences in stress distributions are due to

the structural geometry and configuration-specific features, and not a result of inconsistent loading magnitudes.

For the four-point bending test, a type of surface-to-surface contact constraint was used considering the normal and tangential behavior of the rollers in positions with a friction coefficient equal to 0.2 [24,25]. In both the shear and four-point bending tests, a model was constructed using different mesh sizes with C3D8R elements, a convergence study was conducted, and an element size of 10 mm was selected.

In addition to the FE model in ABAQUS, a MATLAB [26] code was used to calculate the deflection of beam elements based on both Bernoulli and Timoshenko beam theories. In Bernoulli beam theory [27], deflection is determined using the longitudinal modulus of elasticity and the effective bending stiffness, calculated via the gamma method, which includes the rolling shear modulus of the cross-section for each configuration. Also, in Timoshenko beam theory [28], the equations involve the net moment of inertia, the rolling shear modulus for each configuration, the total cross-sectional area, and the shear correction factor. A description of the material properties of CLT panels based on C24 lamellas, which were utilized in the FEM model, can be found in Table 1 based on [11,29].

2.5. Shear correction factor

For a CLT panel the shear correction factor κ_s can be analytically calculated according to Eq. 13, as specified in [11].

$$\kappa_s = \frac{\left(\sum (E_i I_i + E_i A_i a_i^2)\right)^2}{\sum G_i b t_i \int_r \frac{S^2(z) I^2(z)}{G(z) b(z)} dz} \tag{13}$$

In this equation the variables are defined as follows: E_i represents the longitudinal modulus of elasticity of layer i , in [N/mm²]; I_i stands for the net moment of inertia of layer i computed in reference to the neutral axis

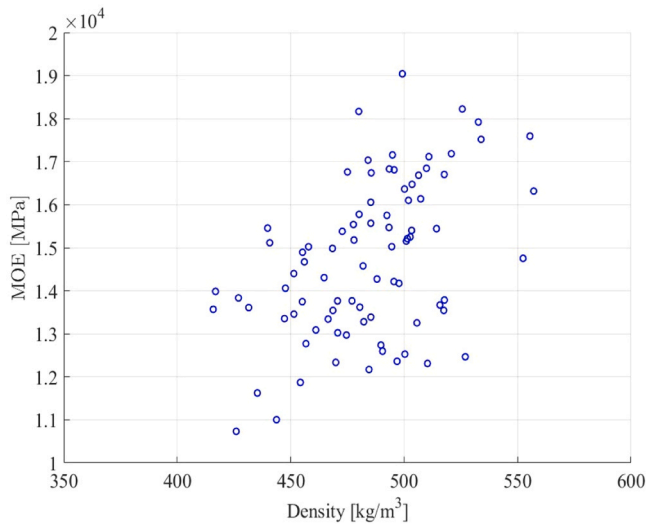


Fig. 8. Relationship between density and MOE of the boards used in producing the shear test specimens.

of layer i , in $[\text{mm}^4]$; A_i is the cross-sectional area of layer i $[\text{mm}^2]$; a_i denotes the distance between the neutral axis of layer i to neutral axis of CLT cross section in $[\text{mm}]$; G_i represents the shear modulus of layer i in $[\text{N}/\text{mm}^2]$; t_i is the thickness of layer i in $[\text{mm}]$; b is the width of the layer in $[\text{mm}]$; $S(z)$ is the first moment of area that depends on coordinate z in $[\text{mm}^3]$; and $G(z)$ is the shear modulus that varies with z in $[\text{N}/\text{mm}^2]$.

In Eq. 13, it is evident that the longitudinal modulus of elasticity (E) does not affect κ under the assumption of a zero-transverse modulus of elasticity. Consequently, the primary factor influencing the shear correction factor for a symmetrically constructed CLT panel is the presence of the rolling shear modulus (G). As indicated in [11], the recommended rolling shear modulus for CLT panels constructed from C24 boards is approximately 50 MPa. An alternative from [15] proposes estimating it as one-tenth of the shear modulus parallel to the grain of the boards.

To assess the influence of these two assumptions on the shear correction factor, a thorough investigation was conducted as follows.

The shear correction factor recommended by Jöbstl for a symmetrical build-up five-layer CLT with equal laminate thickness and with the assumption $\left(\frac{G_{RT}}{G_{LT}} = \frac{1}{10}\right)$ is 0.24 [30]. The analytical solution, detailed in Eq. 13 and plotted against the parameter h_0 (representing the cumulative thickness of longitudinal layers), is presented for a 5-layered CLT panel as shown in Fig. 7a. This visual representation is based on two distinct sets of material properties. The first set draws from C24 specifications, including an assumption where $\left(\frac{G_{RT}}{G_{LT}} = \frac{1}{10}\right)$, with a corresponding rolling shear modulus value of 69 MPa. The second set utilizes material properties specified in [11], with a conventional value of 50 MPa for the rolling shear modulus. Fig. 7b illustrates the relationship between κ and G_{RT} for various values of G_{LT} . The figure also features rings corresponding to the values recommended by Jöbstl for each line. Notably, when the rolling shear modulus is one-tenth of the shear modulus parallel to the grain, it is apparent that the κ value remains consistently close to 0.24 across different GLT values [31,32]. In this study, a rolling shear modulus value of 50 MPa is used as the material property for the transverse layers in both the FEM model and MATLAB calculations for the CLT panel without air gaps (Configuration I). For configurations with air gaps between lamellas in the cross layers, the smeared shear modulus ratio relative to Configuration I is calculated. This ratio is then used to scale the reference value of 50 MPa to assign an effective shear modulus for each configuration. This approach allows the influence of air gaps to be incorporated into the overall shear

performance of the CLT panel.

3. Material properties and design of Configurations

All timber boards used for the shear test specimens were provided with a thickness of 20 mm and were strength-graded as C24 (Spruce). The boards were stored in a conditioning chamber for five months under controlled conditions of $65 \pm 5\%$ relative humidity and a temperature of $20 \pm 2^\circ\text{C}$. This conditioning process resulted in a uniform moisture content of approximately 12 %.

For the shear test, after visual grading, the density of the lamellas was calculated. Following this, the dynamic modulus of elasticity (MOE) in the longitudinal direction was measured using a dynamic vibration test. In this test, the boards were supported on two small cork pieces, a microphone was placed at one end of the board to capture the resonance frequency, while a hardwood hammer was used to strike the opposite end. The first resonance frequency was recorded using FFT analyzer software, and the dynamic MOE in the longitudinal direction was calculated using Eq. 14:

$$MOE_{dyn, long} = 4\rho L^2 f^2 [Pa] \quad (14)$$

The relationship between density and MOE for the boards is presented in Fig. 8. For each CLT configuration in the shear test, four specimens were produced using boards with a mean MOE of 15000 MPa and a mean density of $489 \text{ kg}/\text{m}^3$, with coefficients of variation (COV) of 13 % and 5.7 %, respectively.

Six different configurations of CLT panels were manufactured at Chalmers University of Technology for the shear test. These include a solid panel without air gaps between cross-layers (Configuration I), two configurations with a 6 cm air gap size, one in a central arrangement (Configuration II) and the other in a shifted arrangement (Configuration III), two configurations with a 12 cm air gap size following the same arrangement specifications (Configurations IV and V), and lastly, a configuration with an 8 cm air gap size in a shifted arrangement (Configuration VI), as illustrated in Fig. 9. In addition, the width and height of all specimens were uniformly set to $b = 110 \text{ mm}$ and $t = 100 \text{ mm}$, respectively.

Specimens used in the shear test were fabricated utilizing a polyvinyl acetate (PVAC) adhesive. PVAC glue is characterized by its water solubility, non-toxic nature, and rapid drying, which were found to result in sufficiently strong adhesive bonds for the intended tests. Polyurethane (PUR) adhesives, commonly employed in commercial CLT production, were not utilized due to institutional restrictions prohibiting their use in the lab. Following production and final cutting, the specimens were placed in a climate chamber for a month to undergo reconditioning.

The large-scale specimens used in the four-point bending test were commercially manufactured in an industrial production environment using C24-graded lamellas and polyurethane adhesive. These specimens were subsequently transported to the testing laboratory.

Three distinct configurations of CLT panels were prepared: solid panels without air gaps (Configuration A), and panels with a central arrangement of cross-layers incorporating air gaps of 6 cm (Configuration B) and 12 cm (Configuration C), as illustrated in Fig. 10. All specimens had a consistent width of 200 mm.

As an air gap is introduced in the cross layers, it reduces the overall raw material volume in the panel. The volume ratio (η_v) can be calculated by Eq. 15:

$$\eta_v = \frac{V_{air\ gap}}{V_{solid}} \quad (15)$$

where the $V_{air\ gap}$ is the actual volume of the raw material that is used in a CLT panel with air gaps, and V_{solid} is the apparent volume of the CLT panel. The percentage of material usage can also be referred to as volume ratio. The shear area ratio is determined by dividing the area where shear can occur in specimens with air gaps between cross layers by the

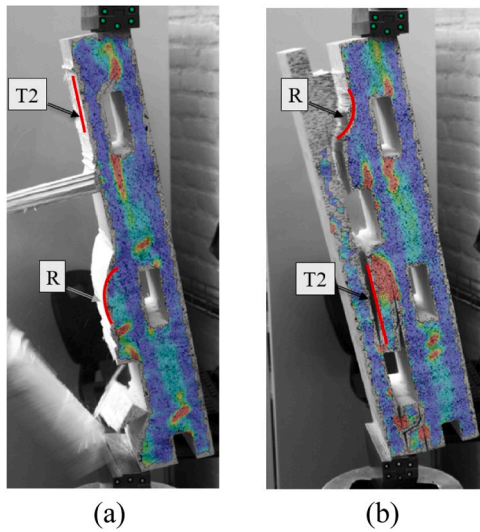


Fig. 12. Failure moment of (a) Sample 2 and (b) Sample 3 in Configuration III, showing two primary failure modes in Sample 3.

Table 3

Summary of the results from the shear tests, including rolling shear strength, smeared shear modulus, and the observed failure mode.

Configuration name	Sample name	f_r	G_{smear}	$f_{r,eff}$	$G_{smear,eff}$	Failure mode
		[MPa]	[MPa]	[MPa]	[MPa]	
I	1	1.29	73.1	1.29	73.1	R, T2
	2	1.27	75.6	1.27	75.6	R, T2
	3	1.12	80.5	1.12	80.5	R, T2
	4	1.56	67.8	1.56	67.8	R, T2
II	1	0.72	45.9	1.08	68.8	R, T2
	2	0.70	44.6	1.05	66.9	R, T2
	3	0.67	39.9	1.01	59.8	R, T2
III	4	0.91	42.7	1.37	64.1	R, T2
	1	0.95	56.6	1.43	84.9	R, T2
	2	0.94	49.4	1.41	74.1	R, T2
IV	3	0.87	57.8	1.31	86.7	R, T2
	4	0.94	41.8	1.41	62.7	T2
	1	0.72	39.6	1.45	79.1	R, T2
	2	0.66	34.9	1.33	69.8	R, T2
V	3	0.61	32.8	1.22	65.7	R, T2
	4	0.71	33.2	1.41	66.4	R, T2
	1	0.68	32.8	1.35	65.6	R, T2
	2	0.43	26.5	0.86	53.0	T2
VI	3	0.49	29.2	0.97	58.5	R, T2
	4	0.68	41.4	1.36	82.9	R, T2
	1	0.81	49.6	1.35	82.7	R, T2
	2	0.70	46.5	1.17	77.6	R, T2
	3	0.77	43.0	1.28	71.7	R, T2
	4	0.92	39.8	1.53	66.4	R

Table 4

The mean values and coefficients of variation for rolling shear strength, shear modulus, and their ratio across different configurations in the shear test, with alignment of η_v and η_A .

Configuration name	η_v	η_A	$f_{r,mean}$ COV	η_f	$G_{smear, mean}$ COV	η_G
	[–]	[–]	[MPa], [%]	[–]	[MPa], [%]	[–]
I	1.00	1.00	1.31, 14.0	1.00	74.3, 7.12	1.00
II	0.87	0.67	0.75, 14.5	0.57	43.3, 6.03	0.58
III	0.87	0.67	0.92, 4.01	0.71	51.4, 14.4	0.69
IV	0.80	0.50	0.67, 7.45	0.52	35.1, 8.88	0.47
V	0.80	0.50	0.57, 22.6	0.44	32.5, 20.0	0.44
VI	0.84	0.60	0.80, 11.5	0.61	44.7, 9.5	0.60

4. Results and discussion

4.1. Shear test results

As an example of a load-deformation curve of the specimens in the shear tests, Fig. 11a presents the load-deformation curve for Configuration III. During the initial phase of load application, the load-displacement relationship is not linear. This non-linearity can be attributed to a manufacturing error that led to an imperfect cutting angle, resulting in an uneven load distribution across the pressure area. Consequently, there was an observed deviation from the linear load-displacement relationship in the early stages of loading. As the load was gradually and consistently distributed over the pressure area, the load-displacement relationship eventually achieved linearity. To consider this non-linear behavior, the calculation of the rolling shear modulus was adjusted to modify the equation specified in EN 408 and EN 789. Specifically, the range between 30 and 60 percent of the maximum load was considered the linear region, replacing the previous range of 10–40 percent.

An example of major strain distribution captured by ARAMIS software at the point of failure load is depicted in Fig. 11b for samples 1, 2, 3 and 4 within Configuration III. It is evident that the maximum strain is observed within the cross-layers, which exhibit a lower shear modulus compared to the longitudinal ones as they are loaded in rolling shear. In addition, the images indicate that strain concentrations are primarily localized at the corners of the air gaps.

Two primary failure mechanisms were identified in this study for the shear tests. The first is denoted as “shear failure” (R) in the radial direction. That happens because of either rolling shear stress in the cross-layer or shear stress parallel to the grain in the longitudinal layer. The second mechanism, referred to as “tension perpendicular to the grain failure” (T2), occurs at the bond line between adjacent boards. This failure is likely driven by a combination of rolling shear stress acting across the full thickness of the CLT panel (captured as a smeared response), localized bending stresses perpendicular to the grain induced by minor eccentricities in the inclined shear test setup, and interlaminar stresses perpendicular to the lamellae. The interaction of these stress components leads to tension perpendicular to the grain at the bond lines, where stress concentrations can develop, particularly near discontinuities such as air gaps, ultimately resulting in the observed failure mode [33].

In solid specimens, initial cracking generally begins in the cross layers and extends into fractures within the wood layer adjacent to the glue line. Consequently, rolling shear failure is observed. In specimens with air gaps, the initial cracks primarily appear at the corners of the air gaps between cross-layers in the bond lines. Subsequently, the cross-layer fails in the region near the air gap between cross-layers, ultimately leading to specimen failure. An example of a moment of failure for samples 2 and 3 for configuration III is presented in Fig. 12.

Table 3 presents a summary of results from shear tests on small specimens, including rolling shear strength (f_r), smeared shear modulus (G_{smear}), and failure mode. Additionally, the effective rolling shear strength ($f_{r,eff}$) and effective smeared shear modulus ($G_{smear,eff}$) are provided. Here, the term ‘effective’ refers to using the bond line length of the actual cross-layers, rather than the total specimen length in Eqs. 2 and 3.

In Table 4, the mean values of rolling shear strength and smeared shear modulus for each configuration are presented, based on the data from four specimens. The ratios for both rolling shear strength (η_f) and smeared shear modulus (η_G) are derived by comparing the shear properties of configurations with air gaps to the solid reference configuration. This comparison is performed by dividing the mean values of the rolling shear strength and modulus observed for the air gap samples by those of the solid samples, as described in Eq. 17.

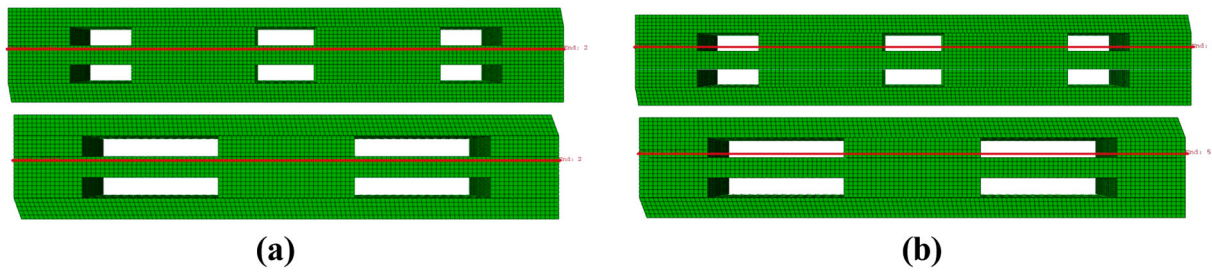


Fig. 13. (a) The location of the path for plotting normal stresses S_{11} , (b) The location of the path for plotting normal stresses S_{22} and shear stresses S_{23} for configurations II and IV.

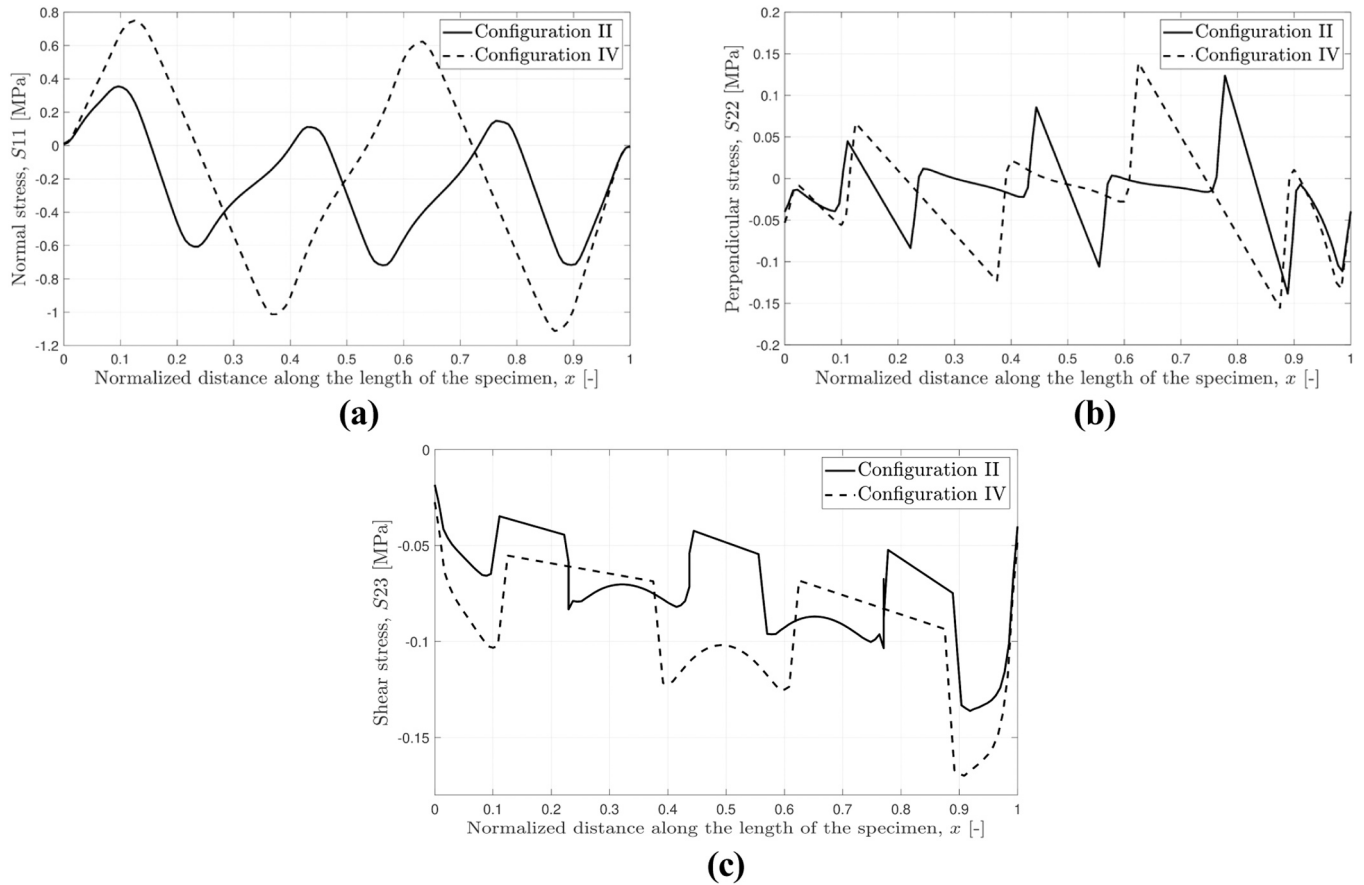


Fig. 14. (a) Comparison of normal stress (S_{11}) plotted along the path at the top of the middle longitudinal layer, (b) Comparison of perpendicular stress (S_{22}) plotted in the middle of the top cross-layer, (c) Comparison of shear stress (S_{23}) plotted in the middle of the top cross-layer, based on results from ABAQUS for Configurations II and IV.

$$\eta_f = \frac{f_{r,airgap}(mean)}{f_{r,solid}(mean)} \quad \eta_G = \frac{G_{smear,airgap}(mean)}{G_{smear,solid}(mean)} \quad (17)$$

4.2. Shear test discussion

Analyzing the outcomes presented in Tables 3 and 4 reveals a consistent pattern. Notably, there is a trend with the rolling shear strength and smeared shear modulus of specimens featuring an air gap consistently being lower than those in solid configurations. Moreover, an increased air gap is consistently associated with a significant reduction in both shear strength and stiffness, as evident in Configuration IV compared to Configuration II. Additionally, configurations featuring shifted arrangements and characterized by cross-layer overlap (S) with values above zero consistently exhibit higher values for both smeared shear modulus and rolling shear strength when compared to the central

arrangement configuration (Configuration III and VI compared to Configuration II). To address research question 1.1., an investigation was conducted on the rolling shear strength ratio and the percentage of material used in CLT panel production, as illustrated in Fig. 18a. Consistent with earlier observations, a decrease in the rolling shear strength of CLT samples is noted with an increase in air gap size.

An interesting aspect is the comparison of the overlap size's effect on rolling shear strength. Significantly, higher rolling shear strength is observed in specimens with overlaps above zero compared to the central arrangement with the same air gap size. However, when the overlap dimensions decrease to zero, lower rolling shear strength is noted compared to the central arrangements of cross layers. This observation is evident in the comparison of Configuration II and III, both having an identical material reduction percentage of 13%. Notably, Configuration III, featuring a cross-layer with overlaps of 3 cm, demonstrated a

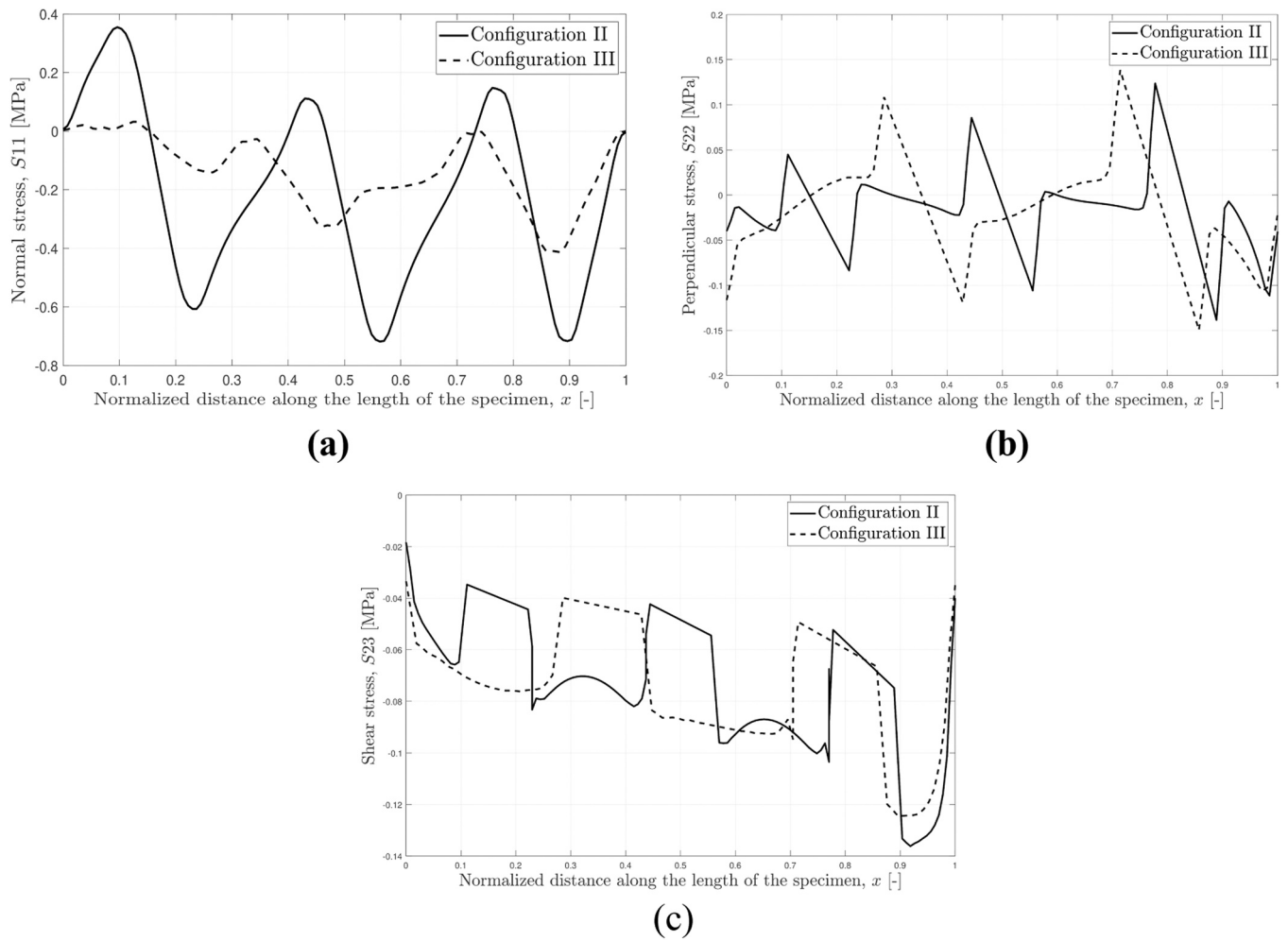


Fig. 15. (a) Comparison of normal stress (S_{11}) plotted along the path at the top of the middle longitudinal layer, (b) Comparison of perpendicular stress (S_{22}) plotted in the middle of the top cross-layer, (c) Comparison of shear stress (S_{23}) plotted in the middle of the top cross-layer, based on results from ABAQUS for Configurations II and III.

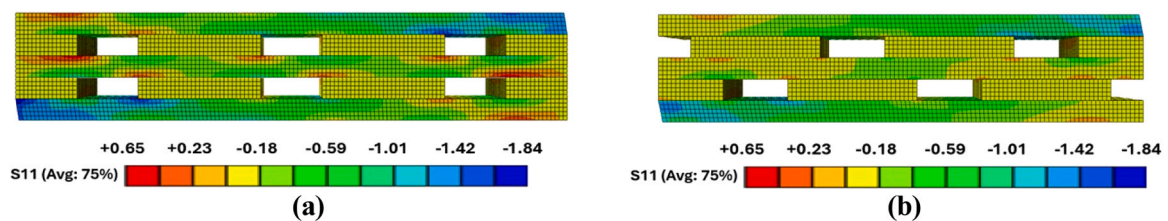


Fig. 16. Distribution of normal stress (S_{11}) for (a) Configuration II, (b) Configuration III, [MPa].

markedly higher rolling shear strength (24 %) than Configuration II. In contrast, Configurations IV and V both incorporated a material reduction of 20 %. Configuration V, characterized by shifted cross layers without any overlap, exhibits lower smeared shear strength than Configuration IV with a central arrangement of cross layers in this case.

The test results were substantiated through finite element (FE) modeling by comparing the stress of different configurations. To ensure consistent loading conditions across specimens with varying geometries, the applied pressure in all FEM simulations was adjusted using the Load Scale Factor (LSF), as defined in Section 2.4. This approach accounts for differences in specimen length and pressure area between configurations, allowing the stress responses to be evaluated under normalized conditions.

The effect of increasing air gap size on stress distribution was

examined through a comparison between Configurations II and IV. This comparison revealed that an increased air gap leads to an increase in maximum stress. In the context of these two configurations, the distribution of normal (S_{11}) and perpendicular and shear (S_{22} , S_{23}) stresses were compared for a path at the upper part of the middle longitudinal layer and at the bottom line of the upper cross-layer edges, as shown in Fig. 13 in the ABAQUS models. Here, S_{11} corresponds to the longitudinal normal stress (σ_L), S_{22} to the radial normal stress (σ_R), and S_{23} to the radial-tangential shear stress (τ_{RT}).

This comparison indicates that the normal stress is twice as high in Configuration IV, characterized by 12 cm wide air gaps when compared to Configuration II, featuring 6 cm wide air gaps. Furthermore, perpendicular and shear stresses exhibit higher values in Configuration IV compared to Configuration II, as depicted in Fig. 14.

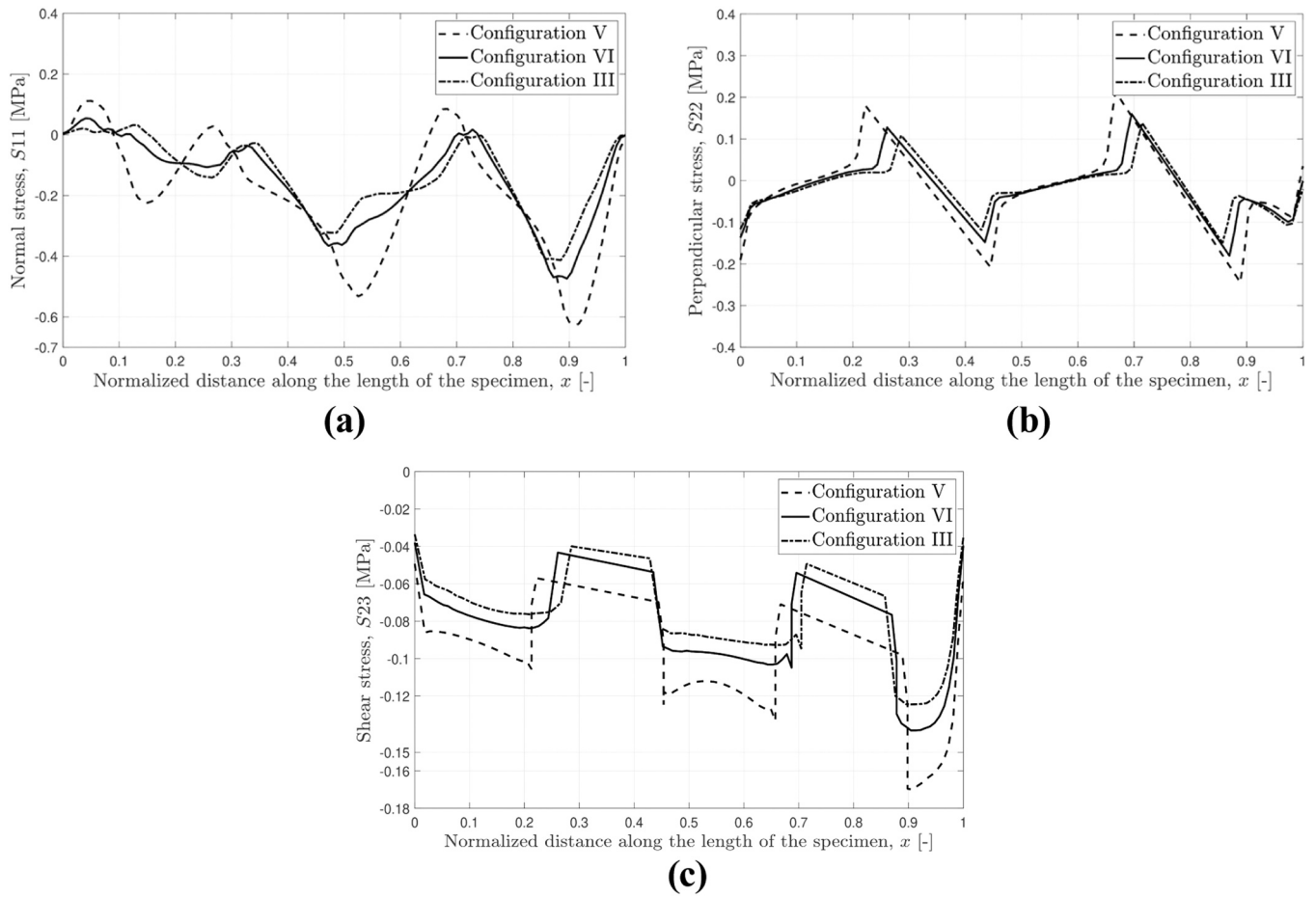


Fig. 17. (a) Comparison of normal stress (S_{11}) plotted along the path at the top of the middle longitudinal layer, (b) Comparison of perpendicular stress (S_{22}) plotted in the middle of the top cross-layer, (c) Comparison of shear stress (S_{23}) plotted in the middle of the top cross-layer, based on results from ABAQUS for Configuration III, V, and VI.

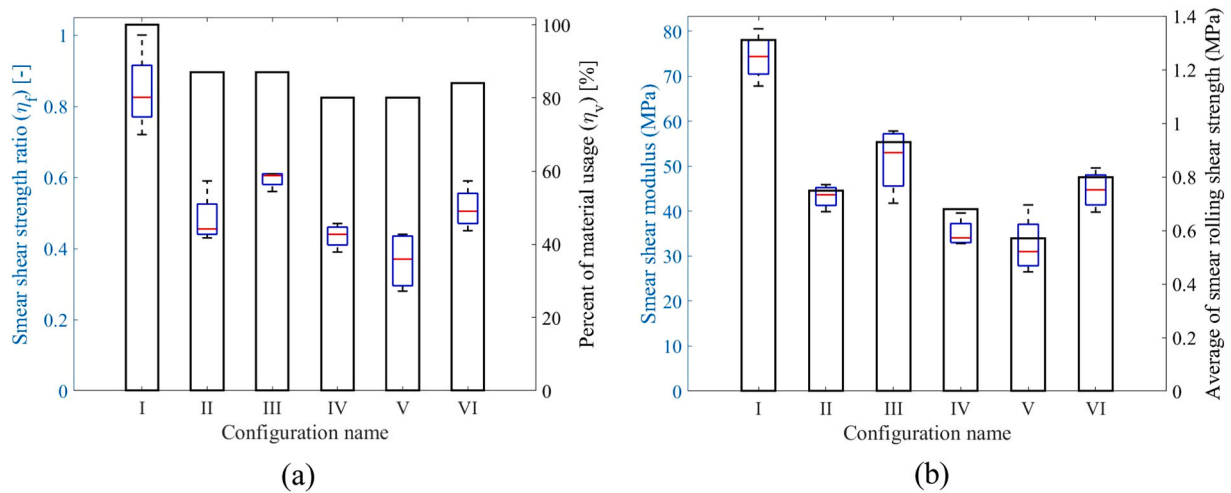


Fig. 18. (a) Comparison of rolling shear strength ratio (box plot, left y-axis) and percent of material usage (right y-axis) for the different configurations, (b) Comparison of smeared shear modulus (box plot, left y-axis) and average rolling shear strength (right y-axis) for the different configurations.

To see the impact of the shifted arrangement on the stress distribution, Configurations II and III with the same air gap size are compared, and the same comparison as explained for Configurations II and IV is employed. As it is clear in Figure 15a, the stress fluctuated less in Configuration III compared to Configuration II. In Configuration III, near the corner where the load is applied on the right side, there is a notable

compression stress. This compression stress diminishes as the distance from the applied load increases, reaching almost zero on the opposite side. Conversely, in Configuration II, stress fluctuates between tension and compression, with a significant increase in tensile stress on the opposite side. An intriguing observation is that in Configuration III, there is almost no area with tension stress, while in Configuration II, the

Table 5

Adjusted smeared shear modulus and shear correction factors for the tested configurations.

Configuration name	I	II	III	IV	V	VI
G_{RT}	50	29	34.5	23.5	22	30
κ_s	0.183	0.111	0.131	0.091	0.086	0.115

stress sign changes at the front edge of an air gap. Moreover, the analysis of perpendicular stress (S_{22}) and shear stress (S_{23}) indicates almost identical stress ranges and shapes in both configurations, albeit consistently higher, as depicted in Figs. 15b, and 15c.

Additionally, the stress contour of (S_{11}) for Configurations II and III is shown in Fig. 16. The normal stress magnitude (S_{11}) is significantly greater in Configuration II, where the air gap is centered, compared to Configuration III, where the air gap is shifted. This disparity arises from stress concentration at the corner of the air gaps in Configuration II. In contrast, Configuration III exhibits smoother stress distribution due to the overlap between the cross-layer and longitudinal layer, covering a larger area.

The results from the shear tests indicated that there was an increase in rolling shear strength and modulus by increasing the overlap length between the cross layers in shifted arrangements. This can be observed

by comparing the stress distribution in the finite element model among Configurations V, VI, and III, which have overlap dimensions of zero, two, and three centimeters, respectively. Fig. 17 illustrates that a reduction in overlap length leads to a significant increase in internal stresses. Under normalized loading conditions, the maximum tensile normal stress (S_{11}), shear stress (S_{23}), and perpendicular stress (S_{22}) in Configuration V are approximately 250 %, 36 %, and 54 % higher, respectively, compared to those observed in Configuration III.

To address research question 1.2., an alignment was performed to compare the rolling shear modulus and average rolling shear strength. The results of this investigation reveal that among the configurations featuring air gaps, Configuration III demonstrates the highest average rolling shear modulus and rolling shear strength. This particular configuration incorporates 6 cm shifted air gaps and a 2 cm overlap between the cross layers. However, it should be noted that the rolling shear modulus and rolling shear strength of Configuration III still exhibit a 29 % reduction when compared to the solid configurations. Additionally, this configuration results in a 13 % material savings compared to the solid configuration. Refer to Fig. 18b for further details.

To address Research Question 1.3. regarding the calculation of the rolling shear modulus for configurations with air gaps, the following approach was adopted: The smeared shear modulus ratio (η_G) for each configuration was determined relative to the reference CLT panel without air gaps, which was assigned a baseline value of 50 MPa. These

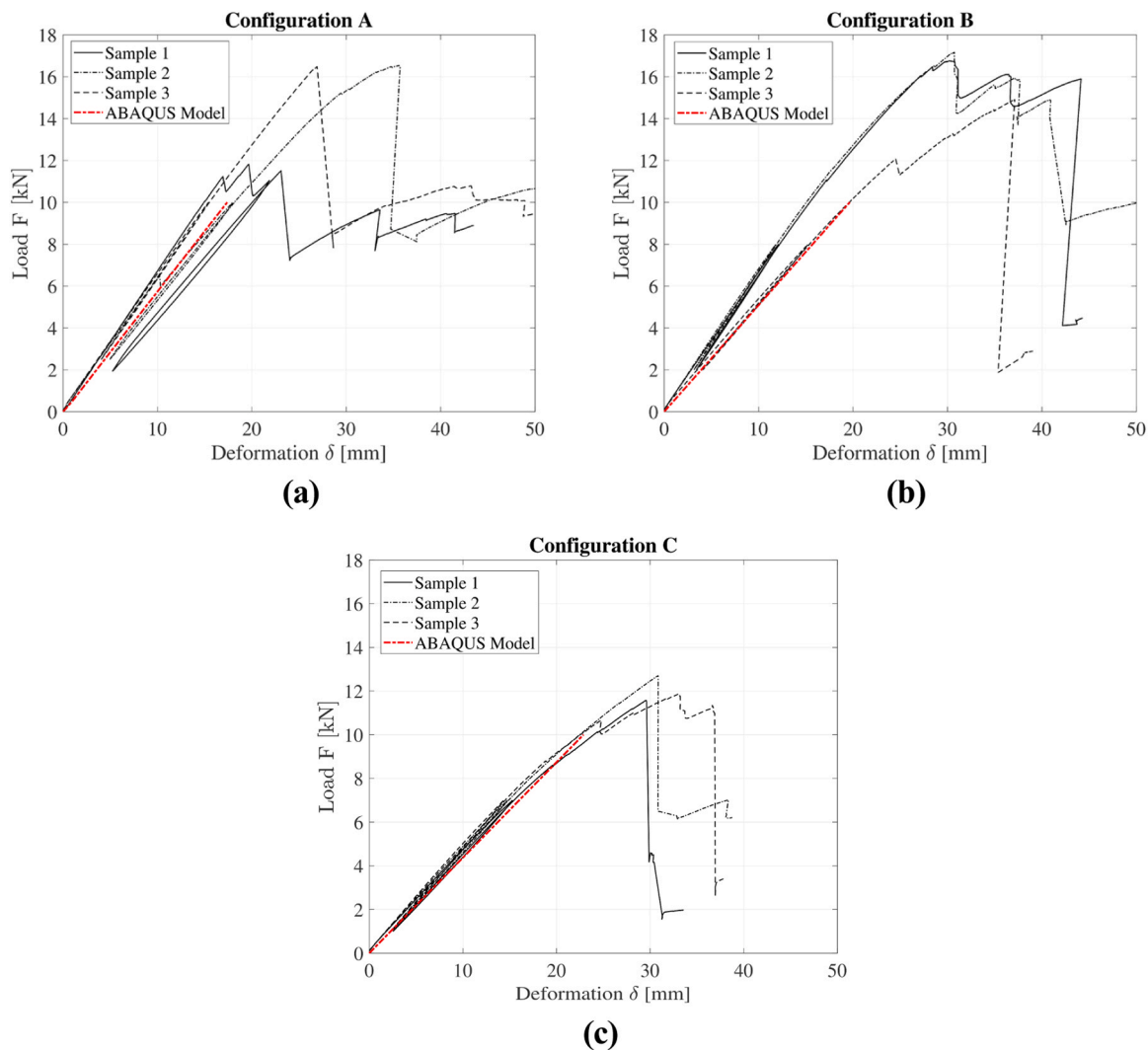


Fig. 19. Load-deformation curves for the midpoint of the panel based on the magnitude of one point load: (a) Configuration A, (b) Configuration B, (c) Configuration C.

Table 6

Summary of bending stiffness calculated based on different methods, and failure modes of the specimens in different configurations.

Configuration	Sample	E^I_{global} , Bernoulli	E^I_{global} , Timoshenko	E^I_{global} , EN408	E^I_{local} , EN789	E^I_{Theory} , eff	E^I_{Theory} , net	Failure mode
name	name	$[\times 10^{10}Nmm^2]$	$[\times 10^{10}Nmm^2]$	$[\times 10^{10}Nmm^2]$	$[\times 10^{10}Nmm^2]$	$[\times 10^{10}Nmm^2]$	$[\times 10^{10}Nmm^2]$	
A	1	14.0	16.9	14.5	16.2	11.5	14.5	Tensile
	2	11.3	13.1	11.7	16.0	11.5	14.5	Tensile
	3	13.4	16.0	13.9	19.6	11.5	14.5	Tensile
B	1	13.5	18.5	14.0	17.6	10.1	14.5	Shear
	2	13.9	19.1	14.4	21.3	10.1	14.5	Shear
	3	10.8	13.7	11.1	14.4	10.1	14.5	Tensile
C	1	9.51	11.3	9.76	12.0	9.47	14.5	Tensile
	2	9.79	11.7	10.0	14.5	9.47	14.5	Tensile
	3	10.1	12.2	10.4	15.4	9.47	14.5	Shear

^a For configurations A, B, and C, κ_s was set to 0.183, 0.111, and 0.091, respectively.



Fig. 20. Test results and failure mode of Sample 1 in the four-point bending test: (a) Configuration A, (b) Configuration B.

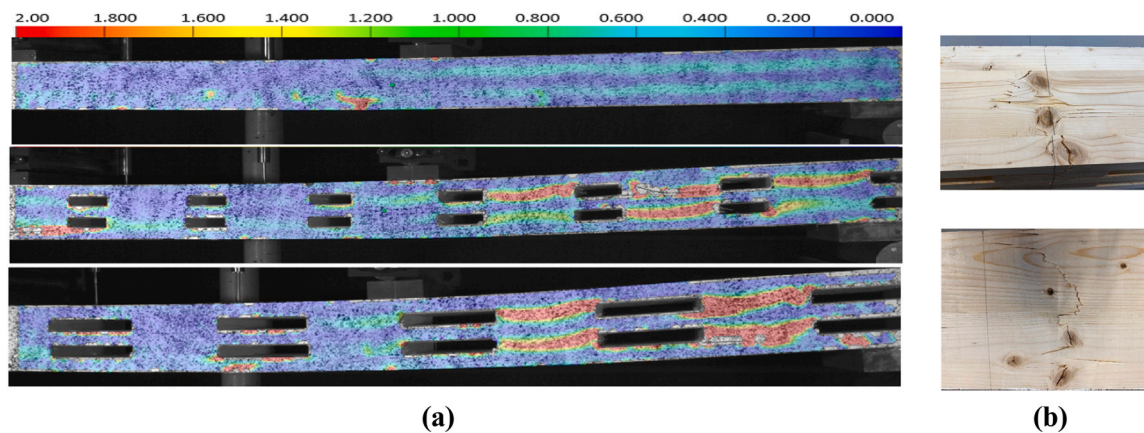


Fig. 21. (a) Major strain [%] distribution (right support to midpoint) for Samples 1, 2, and 3 in Configurations A, B, and C, (b) Tensile failure at the bottom of Sample 1, and Sample 2 of Configuration C.

Table 7

The average of maximum deflections obtained experimentally and through FE calculations (ABAQUS, gamma, and Timoshenko method), under a 5 kN load per loading point, along with corresponding percentage differences from the experiment results.

Configuration	Experimental, COV	ABAQUS	Difference	Gamma method	Difference	Timoshenko method	Difference
name	[mm], [%]	[mm]	[%]	[mm]	[%]	[mm]	[%]
A	7.59, 2.23	8.73	15.0	9.12	20.2	9.16	20.7
B	7.95, 13.8	9.82	23.5	10.4	30.8	10.4	30.7
C	10.2, 2.87	11.44	11.7	11.1	8.59	11.1	8.50

^a For Configurations A, B, and C, κ_s was set to 0.183, 0.113, and 0.093, respectively.

ratios were then used to calculate the effective rolling shear modulus for each configuration. Subsequently, the shear correction factor (κ_s) was recalculated using Eq. 13, incorporating the modified shear modulus values for the cross layers. The resulting values of effective shear modulus and corresponding shear correction factors for all configurations are presented in Table 5.

4.3. Four-point bending test results

As an overview of the four-point bending test, the load-deformation curves along with the responses from the elastic FE model in ABAQUS for Configurations A, B, and C are presented, in Fig. 19. Also in Fig. 21a, the strain distribution of Samples 1, 2, and 3 from Configurations A, B, and C is displayed at the point of failure. Complementing this graphical representation, the global and local flexural stiffness values were determined from the test results through Eqs. 4, 5, 6, and 7, as shown in

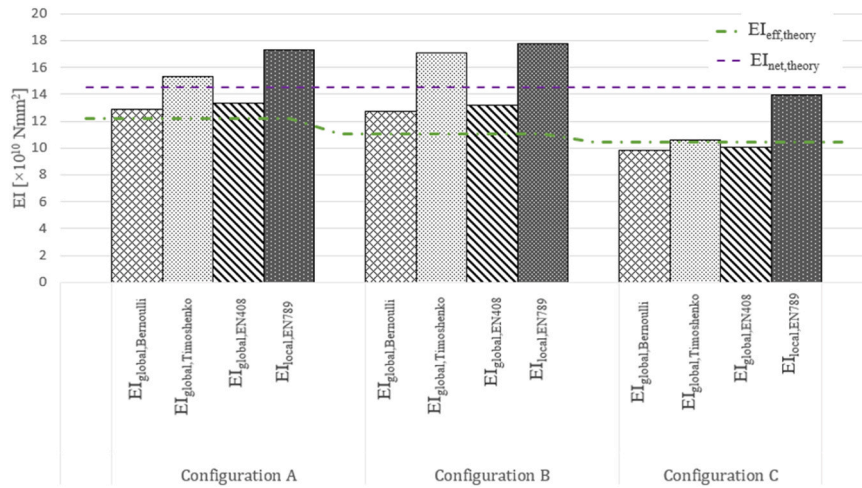


Fig. 22. Comparison of average bending stiffness of each configuration calculated based on different methods.

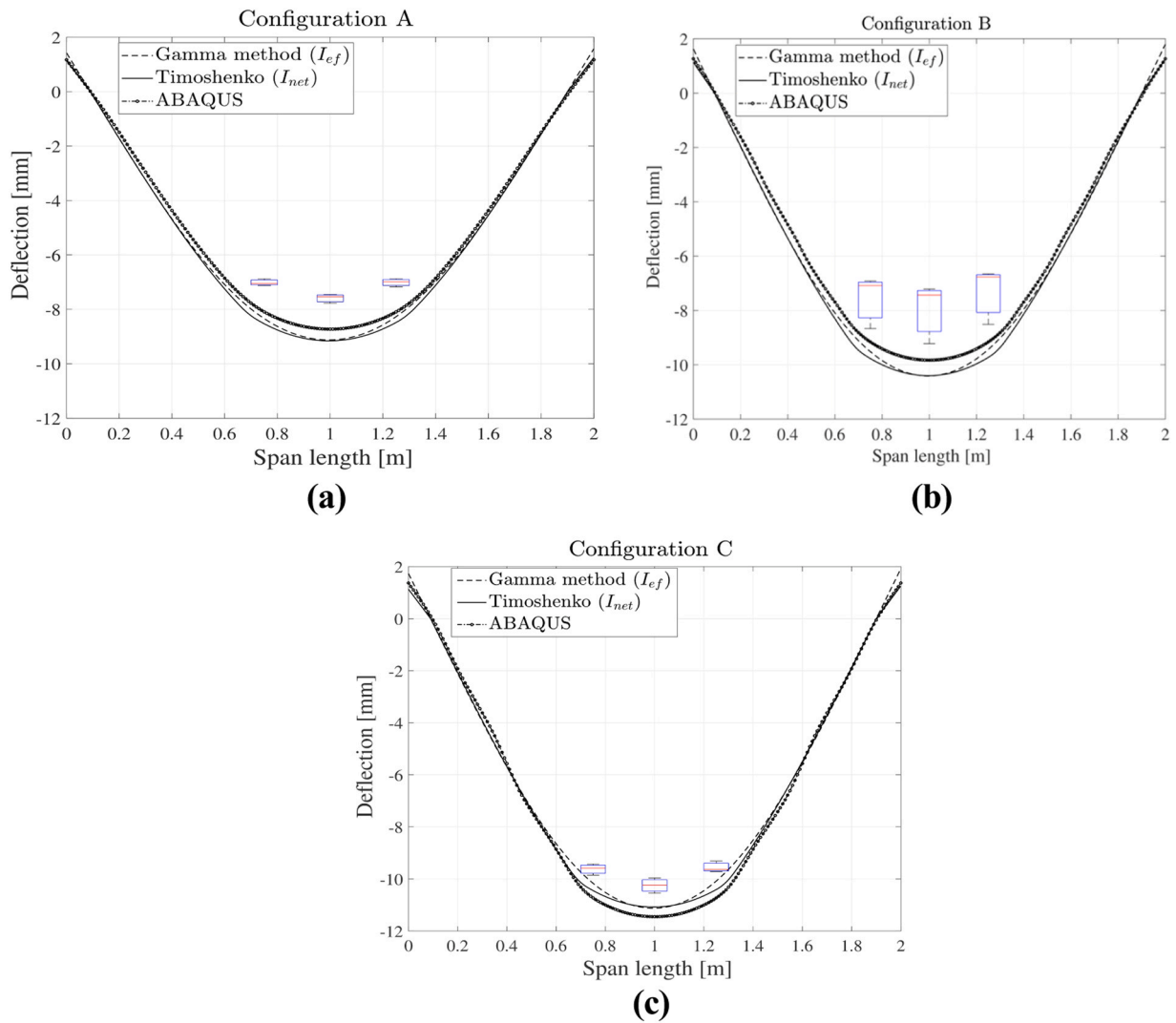


Fig. 23. Comparison of deflections in a CLT beam utilizing MATLAB (Gamma and Timoshenko), ABAQUS simulations, and experimental data (depicted in a box plot): (a) Configuration A, (b) Configuration B, (c) Configuration C. The applied load per loading point in the four-point bending test was 5 KN.

Table 6. Additionally, the failure mode of each sample is indicated in this table.

Furthermore, the theoretical stiffness values of the CLT panels

(EI_{Theory}) were calculated analytically. For that, the effective moment of inertia was computed via the gamma method, and the net moment of inertia was obtained from the Timoshenko method. The parameters

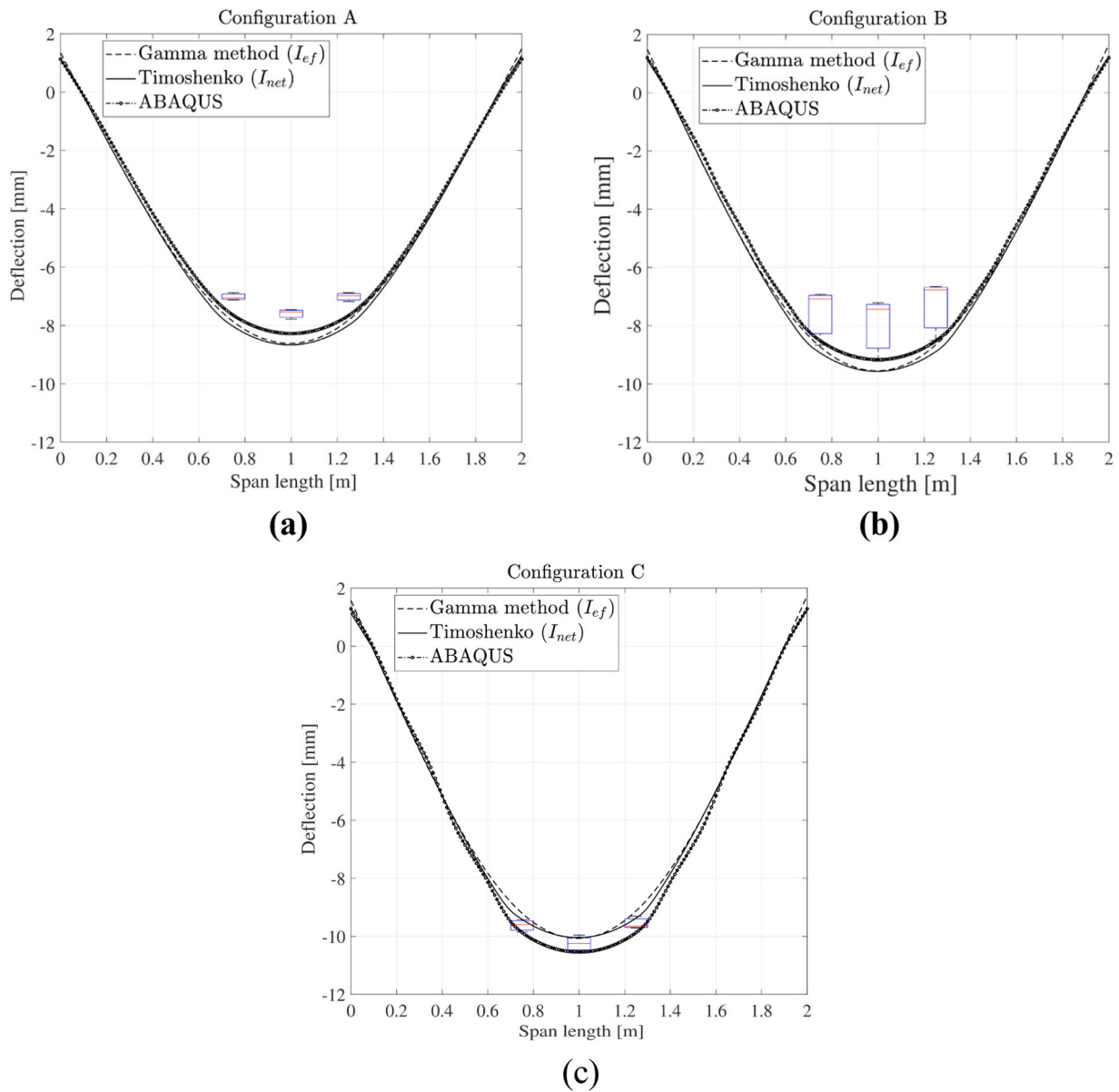


Fig. 24. Comparing deflections of a CLT beam using MATLAB, ABAQUS, and experimental data (depicted in a box plot): (a) Configuration A, (b) Configuration B, (c) Configuration C. The beam, with a width of 0.2 m, underwent four-point bending under a 5 kN load per loading point, with the rolling shear modulus equal to 69 MPa.

input in the corresponding equation in these two methods are explained in 2.4. These inertia values were then multiplied by the reference longitudinal modulus of elasticity, $E_L = 11,000$ (MPa), as listed in Table 1, see Eq. 18.

$$(EI)_{Theory,eff} = E_L \cdot I_{eff} \quad (EI)_{Theory,net} = E_L \cdot I_{net} \quad (18)$$

In the four-point bending test, two principal failure modes were observed: bending and shear failures. Bending causes the dispersion of tension and compression stress throughout the material’s cross-sectional depth, with tension stress leading to brittle failure due to wood fiber rupture that is called tensile failure in this paper. Conversely, shear failure encompasses fiber displacement, resulting in parallel grain cracking, designated as shear failure in this research [34]. As an example, the failure modes for samples 1 from configurations A and B are presented in Fig. 20.

As a result of stress concentration at the corner of the air gap between cross layers, it was expected that the failure mode be a shear failure while for one sample in Configuration B and two samples in

Configuration C, the tensile failure happened. The reason for this behavior is due to the existence of knots and knot clusters at the outermost longitudinal layer in tension, leading to the failure in tensile behavior, see Fig 21b.

Additionally, the deflection of the panels was calculated by means of a simple model in MATLAB in a four-point bending test by utilizing the shear correction factor and rolling shear modulus for configurations with air gaps, employing the corresponding equations in the gamma and Timoshenko methods. The results, depicting the maximum beam deflection under a 5 kN load per loading point, alongside the experimentally obtained data and finite element calculations conducted in ABAQUS, accompanied by their respective percentage differences, are presented in Table 7.

4.4. Four-point bending test discussion

The presented results reveal several key observations: The introduction and enlargement of air gaps lead to increased strain across the

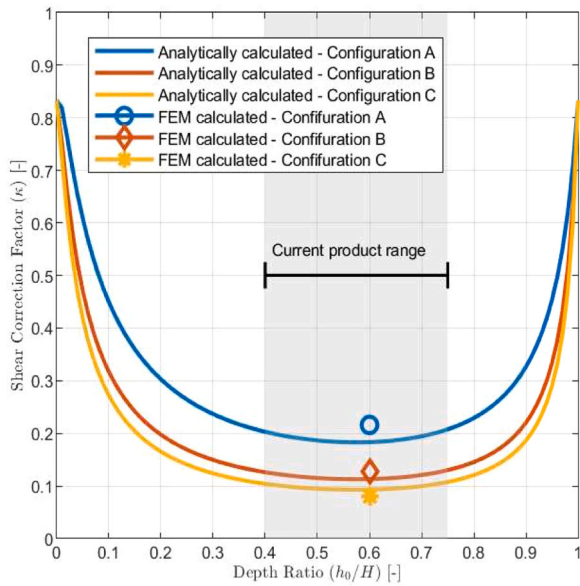


Fig. 25. Comparison between FEM and Analytical calculations of the shear correction coefficient. h_0 represents the cumulative thickness of longitudinal layers. The current product range is calculated based on the data from [11].

cross layers, accompanied by a significant reduction in stiffness, resulting in increased deflection. To address research question 2.1., the average stiffness of each configuration was calculated based on Eqs. 4–7. This calculated stiffness was then compared with the analytical approximation of stiffness, as illustrated in Table 6 and Fig. 22. A conservative orientation in stiffness predictions is observed when determining effective stiffness ($EI_{eff,theory}$) through the gamma method and incorporating the adapted rolling shear modulus into the relevant equations. Also, it is evident that in Configuration B, where air gaps are introduced and the material reduction is 13 %, the calculated bending stiffness values closely resemble those of solid specimens. Conversely, Configuration C, with 12 cm air gaps and a material reduction of about 20 %, experiences a considerable decrease in bending stiffness. The disparity between solid specimens and Configuration C ranges from 19 % to 25 %, depending on the method employed to calculate bending stiffness.

In response to research question 2.2., the deflection behavior of the beam during the four-point bending test was examined using various methodologies, including the gamma method, Timoshenko method, data derived from the ABAQUS FEM model, and their integration with experimental test results. The calculation of deflection using the Timoshenko method involved incorporating a modified shear modulus and an analytically derived shear correction factor.

As shown in Fig. 23, the analysis revealed that the deflection predictions calculated by the gamma method exhibited only a minor difference compared to those obtained using the Timoshenko method, as expected due to $\frac{h_{CLT}}{h_{CLT}} \geq 15$ which equals 20 in this test setup.

The deflection curves were revisited based on the assumption $\left(\frac{G_{RT}}{G_{LT}} = \frac{1}{10}\right)$, considering a presumed rolling shear modulus of 69 MPa for solid CLT panels, as illustrated in Fig. 24. This specific value was utilized in both the FEM models within ABAQUS and MATLAB. Consequently, a noticeable correlation was observed between the updated results and the experimental test outcomes. Particularly, configuration C, distinguished by a larger air gap size, demonstrated a significantly close similarity between the outcomes derived from the Gamma and Timoshenko methods and the FEM model in ABAQUS when compared to the experimental results. Therefore, it is inferred that the value of 50 MPa serves

as a conservative estimate for the rolling shear modulus of a solid CLT panel, a notion also supported in [32].

Finally, the shear correction factor can be calculated based on the FEM model results. This was done by using the Eqs. 8 and 9, and inserting the deflection calculated by the FE model in ABAQUS in Eq. 19.

$$\kappa_s = \frac{Fl_2}{\sum_{i=1}^n A_i G_i \left(w_{global} - \frac{Fl_2 \cdot (3l_2^2 - 4l_2^3)}{24 \cdot E_i \cdot I_{net}} \right)} \quad (19)$$

Taking into account the results from the shear tests and the analytically calculated shear correction factors, this factor can be compared with the results obtained from the ABAQUS model and computed using Eq. 19. It can be seen that the results from the FEM model in ABAQUS are close to the values calculated by Eq. 13.

5. Conclusion and need for further research

This study has conducted a thorough analysis of the structural behavior of Cross Laminated Timber (CLT) panels incorporating air gaps in their cross-layers. Through a combination of numerical analysis and experimental tests, the research evaluated the impact of air gaps on critical aspects such as rolling shear strength, smeared shear modulus, bending stiffness, and deflection behavior of CLT panels.

The results show that the introduction of air gaps significantly influences the structural performance of CLT panels. Configurations with shifted layers and greater overlap between cross layers demonstrated enhanced overall shear modulus and rolling shear strength compared to those with centrally positioned air gaps. This is a vital consideration for optimizing CLT panel design, as strategic placement of air gaps can improve material efficiency without significantly undermining structural integrity.

The study also found that larger air gaps lead to greater deflection and reduced stiffness, highlighting the importance of air gap size in overall CLT panel performance. The modified gamma method, integrating adjusted smeared shear modulus values, was effective in predicting the stiffness of CLT panels with air gaps. The Timoshenko method, however, required an adjustment of the shear correction factor for accurate beam deflection estimation.

These findings underscore the potential of CLT panels with air gaps as a more sustainable option in building materials. While introducing air gaps alters the raw material usage in CLT panel production, it might not directly translate into cost reductions due to various influencing factors in production. Nevertheless, such panels can contribute to minimizing the environmental impacts of the construction industry. Thus, optimizing material use in CLT panels with air gaps presents both challenges and opportunities in sustainable construction practices.

In conclusion, CLT panels with air gaps emerge as a viable alternative to traditional CLT panels. They offer optimized structural performance and efficient material use, suggesting sustainability benefits. These panels represent an innovative solution for future construction projects, balancing structural integrity with material usage. The insights gained from this research are crucial for developing new standards and methodologies in CLT panel design and promoting environmentally responsible construction practices.

Further research is necessary to identify the most effective configurations of cross-layers with air gaps in CLT panels. Optimizing overlapping dimensions could potentially lead to material savings and improved performance. Examining the structural response of panels with different air gap sizes and layer counts is also vital. Additionally, future studies should explore alternative configurations and assess the long-term behavior and durability of CLT panels with air gaps. While this study does not address the potential impacts of large regular gaps on connections and building physics, these are critical areas for future research. Such studies are essential to refine design standards and methodologies, thereby facilitating the adoption of CLT panels as a

sustainable building solution.

CRedit authorship contribution statement

Kurzawinska Hanna: Writing – original draft, Methodology, Investigation, Formal analysis. **Tahmasebi Mohammad:** Writing – original draft, Visualization, Methodology, Investigation, Formal analysis. **Goto Yutaka:** Writing – review & editing, Supervision, Project administration, Methodology, Funding acquisition, Conceptualization. **Jockwer Robert:** Writing – review & editing, Supervision, Methodology, Investigation, Funding acquisition, Formal analysis, Data curation, Conceptualization.

Declaration of Competing Interest

The authors declare the following financial interests/personal relationships which may be considered as potential competing interests: Yutaka Goto reports financial support was provided by Swedish Research Council Formas. If there are other authors, they declare that they have no known competing financial interests or personal relationships that could have appeared to influence the work reported in this paper.

Acknowledgements

The authors express the acknowledgment to The Swedish Research Council for Sustainable Development FORMAS for the research grant (Registration Number 2020-01784) and to Stora Enso for the technical support for the specimen production and feedback to the project from the industrial perspective.

Data Availability

Data will be made available on request.

References

- [1] V. De Araujo, F. Aguiar, P. Jardim, F. Mascarenhas, L. Marini, V. Aquino, H. Santos, T. Panzera, F. Lahr, A. Christoforo, Is cross-laminated timber (CLT) a wood panel, a building, or a construction system? A systematic review on its functions, characteristics, performances, and applications, *Forests* 14 (2) (2023), <https://doi.org/10.3390/f14020264>.
- [2] R. Brandner, G. Flatscher, A. Ringhofer, G. Schickhofer, A. Thiel, Cross-laminated timber (CLT): overview and development, *Eur. J. Wood Wood Prod.* 74 (2016) 331–351, <https://doi.org/10.1007/s00107-015-0999-5>.
- [3] G. Fink, J. Kohler, R. Brandner, Application of European design principles to cross-laminated timber, *Eng. Struct.* 171 (2018) 934–943, <https://doi.org/10.1016/j.engstruct.2018.02.081>.
- [4] B. Toosi. Cross-laminated timber: The market opportunities in North America. Canada: FP Innovations, May 12th (2011).
- [5] R. Anderson, California Assessment of Wood Business Innovation Opportunities and Markets (2015), <https://doi.org/10.13140/RG.2.1.4372.7121>.
- [6] L. Franzoni, A. Lebé, F. Lyon, G. Foret, Influence of orientation and number of layers on the elastic response and failure modes on CLT floors: modeling and parameter studies, *Eur. J. Wood Wood Prod.* 74 (2016) 671–684, <https://doi.org/10.1007/s00107-016-1038-x>.
- [7] G. Silly, A. Thiel, M. Augustin, Options for the resource optimized production of Laminar load carrying members based on wood products, *World Conf. Timber Eng. (WCTE): Vienna, Austria* (2016) 1320–1322.
- [8] P. Fellmoser, H.J. Blaß, Influence of rolling shear modulus on strength and stiffness of structural bonded timber elements, *CIB-W18 Meet.* 37 (2004).
- [9] X. Li, M. Subhani, M. Ashraf, B. Kafle, P. Kremer, A current-state-of-the-art on design rules vs test resistance of cross laminated timber members subjected to transverse loading, *CIGOS 2019 Innov. Sustain. Infrastruct.: Proc. 5th Int. Conf. Geotech. Civ. Eng. Works Struct.* (2020) 185–190, https://doi.org/10.1007/978-981-15-0802-8_26.
- [10] V. Bajzecerová, Bending stiffness of CLT-concrete composite members-comparison of simplified calculation methods, *Procedia Eng.* 190 (2017) 15–20, <https://doi.org/10.1016/j.proeng.2017.05.301>.
- [11] A. Gustafsson, R. Crocetti, A. Just, P. Landel, J. Olsson, A. Pousette, M. Silfverhielm, B. Östman, *The CLT Handbook: CLT structures-facts and planning*, ISBN: 978-91-983214-4-3, First (2019). ISBN: 978-91-983214-4-3.
- [12] S. Timoshenko, LXVI. On the correction for shear of the differential equation for transverse vibrations of prismatic bars, *Lond. Edinb. Dublin Philos. - Sophysical Mag. J. Sci.* 41 (245) (1921) 744–746, <https://doi.org/10.1080/14786442108636264>.
- [13] G. Cowper, The shear coefficient in Timoshenko's beam theory, *J. Appl. Mech.* 33 (2) (1966) 335–340, <https://doi.org/10.1115/1.3625046>.
- [14] A. Thiel, G. Schickhofer, *CLTdesigner—a software tool for designing cross laminated timber elements: 1D-plate-design*, *World Conference on Timber Engineering, Italy* (2010).
- [15] E. Karacabeyli and S. Gagnon. *Canadian CLT handbook*. 2019. ISBN: 978-0-86488-592-0. FPInnovations, 2019.
- [16] T. Bogensperger, G. Silly, and G. Schickhofer. Comparison of methods of approximate verification procedures for cross-laminated timber. Institute for Timber Engineering and Wood Technology Management. Research Report, Holzbau Forschungs gmbh, Graz, Austria (2012).
- [17] M. Jeleč, V. Rajčić, *Cross-laminated timber (CLT)—a state-of-the-art report*, *Dradevinar* 70. 02. (2018) 75–95.
- [18] P. Mayencourt, C. Mueller, Structural optimization of cross-laminated timber panels in one-way bending, *Structures* 18 (2018) 48–59, <https://doi.org/10.1016/j.istruc.2018.12.009>.
- [19] B. EN, et al., *Timber structures—cross-laminated timber—requirements*, EN 16351, in: *Standard*, 2015, *European Standard*, 2015.
- [20] B. EN et al. EN 408: 2010+ A1: 2012. *Timber structures. Structural timber and glued laminated timber. Determination of some physical and mechanical properties*. *Standard*. *European Standard*, 2012.
- [21] H. Andersen, J. Casal, A. Dandrieux, B. Debray, V. De Dianous, N. Duijm, C. Delvosalle, C. Fievez, L. Goossens, R. Gowland, et al., *ARAMIS Final Use Guide* 130 (2006).
- [22] EN 789, *Timber structures—Test methods—Determination of mechanical properties of wood based panels*. *Standard*. *European Standard*, 2004.
- [23] ABAQUS / Standard User's Manual, Version 2020. Dassault Systèmes Simulia Corp, 2020.
- [24] R. Koubek, K. Dedicova, *FRICT. wood Steel* (2014).
- [25] B. Xu, A. Bouchaïr, P. Racher, Analytical study and finite element modelling of timber connections with glued-in rods in bending, *Constr. Build. Mater.* 34 (2012) 337–345, <https://doi.org/10.1016/j.conbuildmat.2012.02.087>.
- [26] MATLAB 9.7.0.1190202 (R2019b). MathWorks Inc., 2019.
- [27] I. Christovasilis, M. Brunetti, M. Follesa, M. Nocetti, D. Vassallo, Evaluation of the mechanical properties of cross-laminated timber with elementary beam theories, *Constr. Build. Mater.* 122 (2016) 202–213, <https://doi.org/10.1016/j.conbuildmat.2016.06.082>.
- [28] M.T. Rahman, M. Ashraf, K. Ghabraie, M. Subhani, Evaluating timoshenko method for analyzing CLT under out-of-plane loading, *Buildings* 10 (2020), <https://doi.org/10.3390/buildings10100184>.
- [29] P. Niemz, D. Caduff, Untersuchungen zur Bestimmung der Poissonschen Konstanten an Fichtenholz, *Holz als Roh-und Werkst.* 66 (1) (2008) 1–4, <https://doi.org/10.1007/s00107-007-0188-2>.
- [30] H.J. Blaß, C. Sandhaas, *Timber engineering*, *Princ. Des. KIT Sci. Publ.* (2017), <https://doi.org/10.5445/KSP/1000069616>.
- [31] M. Wallner-Novak, J. Koppelhuber, K. Pock, *Cross-laminated timber structural design - Basic design and engineering principles according to Eurocode*. *ProHolz: Innsbruck, Austria* (2014) 181.
- [32] E. Nilsson. Characterisation of Cross Laminated Timber Properties. ISSN: 0281-6679. MA thesis. Master Dissertation. 2021. url: (<https://www.byggmek.lth.se>), 2021.
- [33] G. Hochreiner, J. Füssl, J. Eberhardsteiner, S. Aicher, CLT plates under concentrated loading – experimental identification of crack modes and corresponding failure mechanisms. *Materials and Joints in Timber Structures: Recent Developments of Technology*, Springer. Springer, Netherlands, 2014, pp. 703–712, https://doi.org/10.1007/978-94-007-7811-1_5.63.
- [34] S. Franke, B. Franke, A.M. Harte, Failure modes and reinforcement techniques for timber beams-State of the art, *Constr. Build. Mater.* 97 (2015) 2–13, <https://doi.org/10.1016/j.conbuildmat.2015.06.021>.